Elastic wave-vector decomposition in heterogeneous anisotropic media[a]

Yanadet Sripanich[1], Sergey Fomel[1], Junzhe Sun[1], and Jiubing Cheng[2]
[1] The University of Texas at Austin
[2] Tongji University

ABSTRACT

The goal of wave-mode separation and wave-vector decomposition is to separate full elastic wavefield into three wavefields with each corresponding to a different wave mode. This allows elastic reverse-time migration to handle of each wave mode independently . Several of the previously proposed methods to accomplish this task require the knowledge of the polarization vectors of all three wave modes in a given anisotropic medium. We propose a wave-vector decomposition method where the wavefield is decomposed in the wavenumber domain via the analytical decomposition operator with improved computational efficiency using low-rank approximations. The method is applicable for general heterogeneous anisotropic media. To apply the proposed method in low-symmetry anisotropic media such as orthorhombic, monoclinic, and triclinic, we define the two S modes by sorting them based on their phase velocities (S1 and S2), which are defined everywhere except at the singularities. The singularities can be located using an analytical condition derived from the exact phase-velocity expressions for S waves. This condition defines a weight function, which can be applied to attenuate the planar artifacts caused by the local discontinuity of polarization vectors at the singularities. The amplitude information lost because of weighting can be recovered using the technique of local signal-noise orthogonalization. Numerical examples show that the proposed approach provides an effective decomposition method for all wave modes in heterogeneous, strongly anisotropic media.

INTRODUCTION

In seismic imaging by elastic reverse-time migration (RTM), different seismic wave modes generally need to be decoupled. Wave-mode separation in isotropic media is relatively simple to accomplish by means of the divergence and curl operators (Aki and Richards, 2002). Dellinger and Etgen (1990) extended this concept to 2D anisotropic media by projecting the vector wavefield onto the polarization vectors found by solving the Christoffel equation. Yan and Sava (2008) applied wave-mode separation for

elastic RTM in isotropic media. Yan and Sava (2009) addressed *wave-mode separation* in the space domain via the use of non-stationary spatial filters, which enable handling of heterogeneity. They later improved this method by frequency-domain phase-shift plus interpolation (PSPI) technique, which increases the computational efficiency (Yan and Sava, 2011), and extended the application to the case of transversely isotropic media with tilted symmetry axis (TTI) (Yan and Sava, 2012). Alternatively, Zhang and McMechan (2010) developed the *wave-vector decomposition* method originally studied by Dellinger (1991) and successfully appiled this method to transversely isotropic media with vertical symmetry axis (VTI). The wave-vector decomposition is based on the principle of projecting wavefields onto polarization vectors in the wavenumber domain (Dellinger, 1991).

In both wave-mode separation and wave-vector decomposition, the computational cost presents a primary challenge because of the need to solve the Christoffel equation in all phase directions for a given set of stiffness tensor coefficients at each spatial location of the medium. Cheng and Fomel (2014) proposed to reformulate the separation and decomposition operators as Fourier Integral Operators (FIO) and applied the low-rank approximation approach (Fomel et al., 2013), which significantly improved computational efficiency. As shown by Cheng and Kang (2014, 2016), partial mode separation during extrapolation using the pseudo-pure-mode wave equations also helps improving the efficiency of the procedure.

In recent years, orthorhombic anisotropy has become an important topic of interest in places where a simpler transverse isotropy model becomes insufficient for characterizing the subsurface (Tsvankin, 1997, 2012; Bakulin et al., 2000; Xu et al., 2005; Vasconcelos and Tsvankin, 2006; Grechka, 2009; Thomsen, 2014; Sripanich and Fomel, 2015; Sripanich et al., 2015, 2016). An example of an orthorhombic medium is a sedimentary basin with parallel fractures in a transversely isotropic background (Tsvankin and Grechka, 2011; Thomsen, 2014). Elastic wave phenomena in such media involve three mutually orthogonal symmetry planes and can be described by nine independent stiffness coefficients as opposed to five in the case of TI media. This behavior leads to a higher degree of complexity of velocity and polarization vector characterization in comparison with TI media (Schoenberg and Helbig, 1997). In orthorhombic media, P-wave mode is, generally, well-separated from the S modes because of its higher phase velocity and therefore, P waves can be straightforwardly extracted from the full elastic wavefield (Dellinger, 1991). The S-wave modes, however, are extricably coupled and more difficult to separate (Schoenberg and Helbig, 1997). Dellinger (1991) showed that if the S waves were separated based on the magnitude of their phase velocities (S1 and S2), the resulting wavefields would be plagued with strong planar artifacts associated with the effects of a polarization discontinuity at the singularity, which in the wavenumber domain, behaved similarly to the delta function. Moreover, orthorhombic symmetry is associated with kiss and point singularities but not the intersection singularity observed in the TI case (Crampin and Yedlin, 1981; Crampin, 1984, 1991). The number of kiss and point singularities, and their corresponding phase directions are not fixed and depend on the model parameters. Therefore, a simple global weighting function cannot eliminate artifacts caused

by a discontinuity of polarization vectors as in the case of a kiss singularity along the symmetry axis in TI media (Yan and Sava, 2012).

In this study, we first extend the wave-vector decomposition method using low-rank approximation (Cheng and Fomel, 2014) and apply it to separate elastic wave-field in orthorhombic media, as well as, in monoclinic and triclinic media, where only the effects of kiss and point singularities for S waves are possible. Because the velocity of the P-wave mode in models considered in practice are generally larger than those of the S-wave modes, there is no ambiguity in identifying its polarization from the solution of the Christoffel equation. To distinguish between the two S-wave modes, we follow the definitions of S modes proposed by Dellinger (1991) and separate them into S1 and S2 based on their phase velocities. We subsequently propose a constructive method for locating singularities that can be used for defining a smoothing filter (weighting function) to mitigate the artifacts caused by discontinuities of polarization vectors. We recover from amplitude loss caused by the smoothing filter via the process of local signal-noise orthogonalization (Chen and Fomel, 2015). We test the proposed method with a set of synthetic examples of increasing complexity.

REVIEW OF WAVE-MODE SEPARATION AND WAVE-VECTOR DECOMPOSITION

Elastic wave-mode separation

According to the Helmholtz decomposition theory (Aki and Richards, 2002), a vector wavefield $\mathbf{U} = \{U_x, U_y, U_z\}$ in homogeneous isotropic media can be decomposed into P-wavefield (curl-free) and S-wavefield (divergence-free) components: $\mathbf{U} = \mathbf{U^P} + \mathbf{U^S}$. The wavefield $\mathbf{U^P}$ satisfies

$$\nabla \times \mathbf{U^P} = 0 \quad \text{and} \quad P = \nabla \cdot \mathbf{U} = \nabla \cdot \mathbf{U^P} \ , \tag{1}$$

while $\mathbf{U^S}$ satisfies

$$\nabla \cdot \mathbf{U^S} = 0 \quad \text{and} \quad \mathbf{S} = \nabla \times \mathbf{U} = \nabla \times \mathbf{U^S} \ . \tag{2}$$

In the Fourier domain, the equivalent expressions are

$$\widetilde{P}(\bar{\mathbf{k}}) = i\bar{\mathbf{k}} \cdot \widetilde{\mathbf{U}}(\bar{\mathbf{k}}) \quad \text{and} \quad \widetilde{\mathbf{S}}(\bar{\mathbf{k}}) = i\bar{\mathbf{k}} \times \widetilde{\mathbf{U}}(\bar{\mathbf{k}}) \ , \tag{3}$$

where $\mathbf{k} = \{k_x, k_y, k_z\}$ denotes the wave-vector, and $\bar{\mathbf{k}} = \mathbf{k}/|\mathbf{k}|$ is its normalized quantity, which is similar to the unit phase direction. $\widetilde{P}(\bar{\mathbf{k}})$ and $\widetilde{\mathbf{S}}(\bar{\mathbf{k}})$ represent the scalar P-wavefield and the vector S-wavefield in the Fourier domain respectively. In homogeneous anisotropic media, the P- and S- waves are not polarized parallel and perpendicular to the wave-vector direction ($\mathbf{k}$) and therefore, expressions in equation 3 cannot separate the wavefield correctly. Dellinger and Etgen (1990) modified these operators for separating P and S waves in homogeneous TI media as follows:

$$\widetilde{P}(\bar{\mathbf{k}}) = i\mathbf{a^P}(\bar{\mathbf{k}}) \cdot \widetilde{\mathbf{U}}(\bar{\mathbf{k}}) \quad \text{and} \quad \widetilde{\mathbf{S}}(\bar{\mathbf{k}}) = i\mathbf{a^P}(\bar{\mathbf{k}}) \times \widetilde{\mathbf{U}}(\bar{\mathbf{k}}) \ , \tag{4}$$

where $\mathbf{a^P}(\bar{\mathbf{k}})$ denotes the normalized polarization vector of P wave obtained by solving the Christoffel equation. Note that $\widetilde{\mathbf{S}}(\bar{\mathbf{k}})$ contains the wavefield corresponding to both S-wave modes.

Despite the validity of both operators in equation 4, the first expression has found more uses in practice because of its simplicity (Yan and Sava, 2009). In homogeneous TI media, one can separate scalar SV- and SH-wavefields using the following expressions:

$$\widetilde{SV}(\bar{\mathbf{k}}) = i\mathbf{a^{SV}}(\bar{\mathbf{k}}) \cdot \widetilde{\mathbf{U}}(\bar{\mathbf{k}}) \quad \text{and} \quad \widetilde{SH}(\bar{\mathbf{k}}) = i\mathbf{a^{SH}}(\bar{\mathbf{k}}) \cdot \widetilde{\mathbf{U}}(\bar{\mathbf{k}}) \ , \tag{5}$$

with appropriately defined normalized polarization vectors of $\mathbf{a^{SV}}$ and $\mathbf{a^{SH}}$ from the Christoffel equation. For heterogeneous VTI media, the polarizations become dependent on the spatial locations and can be denoted as $\mathbf{a^P}(\mathbf{x}, \bar{\mathbf{k}})$, $\mathbf{a^{SV}}(\mathbf{x}, \bar{\mathbf{k}})$, and $\mathbf{a^{SH}}(\mathbf{x}, \bar{\mathbf{k}})$ for proper usage in equations 4 and 5.

For efficient implementation in the space domain, Yan and Sava (2009) proposed to approximate these operators in heterogeneous VTI media as non-stationary filters. An application of this process is commonly referred to as *wave-mode separation*. Its extension to heterogeneous TTI media was proposed by Yan and Sava (2012). However, the computational cost for this approach is large as it is proportional to the number of grids in the model and the size of each filter (Yan and Sava, 2011). To cope with S-wave singularities, Yan and Sava (2012) proposed to scale the displacements corresponding to the two S-wave modes by $\sin\theta$, where θ is the polar angle from the symmetry axis. This method produces uniformly scaled elastic wavefields of the two S-wave modes with zero amplitude along the symmetry axis where the kiss singularities are located. As a downside, the final separated scalar wavefields suffer from both 90° phase shift from the i factor and incorrect amplitudes from $\sin\theta$ scaling and may not be applicable to true-amplitude imaging techniques.

Elastic wave-vector decomposition

Wave-vector decomposition aims to decompose wavefields in the wavenumber domain via a projection operator. For homogeneous isotropic media, Zhang and McMechan (2010) proposed to rewrite equations 1 and 2 as

$$\bar{\mathbf{k}} \times \widetilde{\mathbf{U}}^{\mathbf{P}}(\bar{\mathbf{k}}) = 0 \quad \text{and} \quad \bar{\mathbf{k}} \cdot \widetilde{\mathbf{U}}(\bar{\mathbf{k}}) = \bar{\mathbf{k}} \cdot \widetilde{\mathbf{U}}^{\mathbf{P}}(\bar{\mathbf{k}}) \ , \tag{6}$$

and

$$\bar{\mathbf{k}} \cdot \widetilde{\mathbf{U}}^{\mathbf{S}}(\bar{\mathbf{k}}) = 0 \quad \text{and} \quad \bar{\mathbf{k}} \times \widetilde{\mathbf{U}}(\bar{\mathbf{k}}) = \bar{\mathbf{k}} \times \widetilde{\mathbf{U}}^{\mathbf{S}}(\bar{\mathbf{k}}) \ . \tag{7}$$

As follows from equations 6 and 7, the following equivalent expressions are (Zhang and McMechan, 2010)

$$\widetilde{\mathbf{U}}^{\mathbf{P}}(\bar{\mathbf{k}}) = \bar{\mathbf{k}}[\bar{\mathbf{k}} \cdot \widetilde{\mathbf{U}}(\bar{\mathbf{k}})] \ , \tag{8}$$

and

$$\widetilde{\mathbf{U}}^{\mathbf{S}}(\bar{\mathbf{k}}) = -\bar{\mathbf{k}} \times [\bar{\mathbf{k}} \times \widetilde{\mathbf{U}}(\bar{\mathbf{k}})] \ . \tag{9}$$

The expressions corresponding to equations 8 and 9 in homogeneous TI media are

$$\widetilde{\mathbf{U}}^{\mathbf{P}}(\bar{\mathbf{k}}) = \mathbf{a}^{\mathbf{P}}(\bar{\mathbf{k}})[\mathbf{a}^{\mathbf{P}}(\bar{\mathbf{k}}) \cdot \widetilde{\mathbf{U}}(\bar{\mathbf{k}})] \tag{10}$$

and

$$\widetilde{\mathbf{U}}^{\mathbf{S}}(\bar{\mathbf{k}}) = -\mathbf{a}^{\mathbf{P}}(\bar{\mathbf{k}}) \times [\mathbf{a}^{\mathbf{P}}(\bar{\mathbf{k}}) \times \widetilde{\mathbf{U}}(\bar{\mathbf{k}})] \ , \tag{11}$$

where $\widetilde{\mathbf{U}}^{\mathbf{S}}(\bar{\mathbf{k}})$ contains the wavefield corresponding to both S-wave modes. Equation 10 was originally proposed by Dellinger (1991). To decompose a vector wavefield, one can use either equation 10 or equation 11 and polarization vectors obtained from solving the Christoffel equation. Following equation 10, we can decompose the wavefield in a homogeneous TI medium as follows:

$$
\begin{aligned}
\widetilde{\mathbf{U}}^{\mathbf{P}}(\bar{\mathbf{k}}) &= \mathbf{a}^{\mathbf{P}}(\bar{\mathbf{k}})[\mathbf{a}^{\mathbf{P}}(\bar{\mathbf{k}}) \cdot \widetilde{\mathbf{U}}(\bar{\mathbf{k}})] \ , \\
\widetilde{\mathbf{U}}^{\mathbf{SV}}(\bar{\mathbf{k}}) &= \mathbf{a}^{\mathbf{SV}}(\bar{\mathbf{k}})[\mathbf{a}^{\mathbf{SV}}(\bar{\mathbf{k}}) \cdot \widetilde{\mathbf{U}}(\bar{\mathbf{k}})] \ , \\
\widetilde{\mathbf{U}}^{\mathbf{SH}}(\bar{\mathbf{k}}) &= \mathbf{a}^{\mathbf{SH}}(\bar{\mathbf{k}})[\mathbf{a}^{\mathbf{SH}}(\bar{\mathbf{k}}) \cdot \widetilde{\mathbf{U}}(\bar{\mathbf{k}})] \ .
\end{aligned}
\tag{12}
$$

Following equation 11, we can decompose the wavefield in a homogeneous TI medium as follows:

$$
\begin{aligned}
\widetilde{\mathbf{U}}^{\mathbf{S}}(\bar{\mathbf{k}}) &= -\mathbf{a}^{\mathbf{P}}(\bar{\mathbf{k}}) \times [\mathbf{a}^{\mathbf{P}}(\bar{\mathbf{k}}) \times \widetilde{\mathbf{U}}(\bar{\mathbf{k}})] \ , \\
\widetilde{\mathbf{U}}^{\mathbf{SV}}(\bar{\mathbf{k}}) &= -\mathbf{a}^{\mathbf{SH}}(\bar{\mathbf{k}}) \times [\mathbf{a}^{\mathbf{SH}}(\bar{\mathbf{k}}) \times \widetilde{\mathbf{U}}^{\mathbf{S}}(\bar{\mathbf{k}})] \ , \\
\widetilde{\mathbf{U}}^{\mathbf{SH}}(\bar{\mathbf{k}}) &= -\mathbf{a}^{\mathbf{SV}}(\bar{\mathbf{k}}) \times [\mathbf{a}^{\mathbf{SV}}(\bar{\mathbf{k}}) \times \widetilde{\mathbf{U}}^{\mathbf{S}}(\bar{\mathbf{k}})] \ .
\end{aligned}
\tag{13}
$$

The handling of heterogeneity can be done in a similar fashion to the wave-mode separation case where the polarizations become functions of both spatial location and normalized wave-vector. Because the wave-vector decomposition defined in equations 12 and 13 satisfies the linear superposition relation, the three separated wavefields are orthogonal to one another, while their amplitude, phase, and other physical properties are correctly preserved, unlike the results from the wave-mode separation in equations 4 and 5.

To extend the wave-vector decomposition to low-symmetry anisotropic media, we follow the scheme in equation 12 and utitlize the projection operator for the α wave mode given by

$$\widetilde{\mathbf{U}}^{\alpha}(\bar{\mathbf{k}}) = \mathbf{a}^{\alpha}(\mathbf{x}, \bar{\mathbf{k}})[\mathbf{a}^{\alpha}(\mathbf{x}, \bar{\mathbf{k}}) \cdot \widetilde{\mathbf{U}}(\bar{\mathbf{k}})] \ , \tag{14}$$

where the heterogeneity is taken into account via the dependence of the polarization vector $\mathbf{a}^{\alpha}(\mathbf{x}, \bar{\mathbf{k}})$ on spatial location $\mathbf{x}$ and normalized wave-vector $\bar{\mathbf{k}}$. We discuss the suitable definitions of wave modes in low-symmetry anisotropic media in a later section.

Low-rank approximations for wave-vector decomposition operator

For the wave-vector decomposition method, we focus on equation 14 and transform it to the space domain using the inverse Fourier transform as follows (Cheng and Fomel,

2014):

$$\mathbf{U}^\alpha(\mathbf{x}) = \int e^{i\mathbf{k}\cdot\mathbf{x}} \left[\mathbf{a}^\alpha(\mathbf{x},\bar{\mathbf{k}})[\mathbf{a}^\alpha(\mathbf{x},\bar{\mathbf{k}}) \cdot \widetilde{\mathbf{U}}(\bar{\mathbf{k}})] \right] d\mathbf{k} = \int e^{i\mathbf{k}\cdot\mathbf{x}} \left[\mathbf{A}^\alpha(\mathbf{x},\bar{\mathbf{k}})\widetilde{\mathbf{U}}(\bar{\mathbf{k}}) \right] d\mathbf{k} \ , \quad (15)$$

where $\widetilde{\mathbf{U}}(\mathbf{k})$ denotes the unseparated wavefield in the Fourier domain and $\mathbf{U}^\alpha(\mathbf{x})$ denotes the decomposed wavefield of α wave mode in the space domain. Equation 15 indicates that the unseparated wavefield is projected onto polarization vector $\mathbf{a}^\alpha(\mathbf{x},\bar{\mathbf{k}})$ of α wave mode in the Fourier domain and subsequently transformed back to the space domain for the final decomposed wavefield. The elements of matrix $\mathbf{A}^\alpha(\mathbf{x},\bar{\mathbf{k}})$ are given by

$$\mathbf{A}^\alpha(\mathbf{x},\bar{\mathbf{k}}) = \begin{bmatrix} a_x^\alpha a_x^\alpha & a_x^\alpha a_y^\alpha & a_x^\alpha a_z^\alpha \\ a_y^\alpha a_x^\alpha & a_y^\alpha a_y^\alpha & a_y^\alpha a_z^\alpha \\ a_z^\alpha a_x^\alpha & a_z^\alpha a_y^\alpha & a_z^\alpha a_z^\alpha \end{bmatrix} \ , \quad (16)$$

where $\mathbf{a}^\alpha(\mathbf{x},\bar{\mathbf{k}}) = \{a_x^\alpha, a_y^\alpha, a_z^\alpha\}$ and x, y, and z denoting different components.

Applying the low-rank approximation approach (Fomel et al., 2013), each element of $\mathbf{A}^\alpha(\mathbf{x},\bar{\mathbf{k}})$ for a specified α wave mode in equation 15 and 16 can be approximated as follows (Cheng and Fomel, 2014):

$$a_i^\alpha a_j^\alpha = A_{ij}^\alpha(\mathbf{x},\bar{\mathbf{k}}) \approx \sum_{m=1}^{M} \sum_{n=1}^{N} \mathbf{B}(\mathbf{x},\bar{\mathbf{k}}_m)\mathbf{W}_{mn}\mathbf{C}(\mathbf{x}_n,\bar{\mathbf{k}}) \ , \quad (17)$$

where $\mathbf{B}(\mathbf{x},\bar{\mathbf{k}}_m)$ and $\mathbf{C}(\mathbf{x}_n,\bar{\mathbf{k}})$ are mixed-domain matrices with reduced wavenumber and spatial dimensions respectively; $\mathbf{W}_{mn}$ is a $M \times N$ matrix with M and N representing the rank of this low-rank decomposition. One can view $\mathbf{B}$ as a submatrix of A_{ij}^α consisting of columns associated with $\bar{\mathbf{k}}_m$, and $\mathbf{C}$ as a submatrix of A_{ij}^α consisting of rows associated with $\mathbf{x}_n$. Physically, this process means that we only consider a selected few representative spatial locations ($N \ll N_x$) and representative wavenumbers ($M \ll N_x$), where N_x is the size of the model, to build an effective approximation. As a result, the low-rank approximation reduces computational cost by transforming the Fourier integral operator in equation 15 for each component i and j denoting x, y, and z components to

$$\int e^{i\mathbf{k}\cdot\mathbf{x}} A_{ij}^\alpha(\mathbf{x},\bar{\mathbf{k}})\widetilde{U}_j(\mathbf{k})d\mathbf{k} \approx \sum_{m=1}^{M} \mathbf{B}(\mathbf{x},\bar{\mathbf{k}}_m) \left(\sum_{n=1}^{N} \mathbf{W}_{mn} \left(\int e^{i\mathbf{k}\cdot\mathbf{x}} \mathbf{C}(\mathbf{x}_n,\bar{\mathbf{k}})\widetilde{U}_j(\mathbf{k})d\mathbf{k} \right) \right) \ . \quad (18)$$

The computational cost of applying equation 18 is equivalent to the cost of N inverse fast Fourier Transforms (FFT) (Cheng and Fomel, 2014).

qS-WAVE POLARIZATION VECTORS IN HOMOGENEOUS LOW-SYMMETRY ANISOTROPIC MEDIA

The wave-mode separation and wave-vector decomposition methods discussed in the previous sections rely on the knowledge of polarization vectors of wave modes in

anisotropic media. Polarization vectors can be found from the Christoffel equation as described in Appendix A. The directions in which the two S waves have equal phase velocity are referred to as S-wave singularities. In the case of TI media, two kinds of S-wave singularities are possible: kiss and intersection singularities (Crampin and Yedlin, 1981; Crampin, 1984, 1991). The former is located along the symmetry axis, whereas the latter can be located at a non-zero polar angle depending on the values of the stiffness tensor coefficients. The problems of wave-mode separation and wave vector decomposition in this kind of media have been studied previously (Yan and Sava, 2009, 2012; Zhang and McMechan, 2010). The polarization vectors of both S modes rotate rapidly in the vicinity of the kiss singularity, forcing the modes to be coupled. On the other hand, there is no ambiguity in distinguishing between the two S modes at the intersection singularity, because each mode (SV and SH) must have continuous polarization vectors with respect to the change in phase directions and thus, follow different paths on the slowness surface. This behavior at the intersection singularity is similar to that observed when considering a 2D plane cut through a point singularity (Vavryčuk, 2001).

In general, P-wave polarization vectors are close to the phase direction and correspond to the largest phase velocity (Crampin, 1984). Therefore, P wave is generally well-separated from the S waves. Polarization vectors of the two S waves, however, cannot be fully decoupled from each other, which makes them cumbersome to compute. Orthorhombic or anisotropic media of lower symmetry, such as monoclinic or triclinic, can have both the kiss singularity and the third kind of singularity, point (conical) singularity, where the two S-wave slowness surfaces become continuous through the vertices of cone-shaped projections from the surface (Crampin and Yedlin, 1981). In the 2D plane where point singularities occur, the behavior of the two S modes appear similar to that in the case of intersection singularity in TI media (Vavryčuk, 2001). However, in 3D, the slowness surfaces of both S modes do not form a consistent line intersection as in the case of intersection singularity in TI media (Figures 1 and 2) but rather touch at several locations that define S-wave singularities with a rapid rotation of S-wave polarizations around such locations (Figure 3a). Therefore, the generalization of the definitions of SV and SH wave modes from the 2D plane are not valid in orthorhombic or lower-symmetry media (Tsvankin, 2012).

To define the wave modes in such media, we recognize that the three modes must be unique single-valued continuous functions of phase velocity versus phase direction. The most intuitive way to define S modes is to sort them based on the magnitude of the phase velocity (Dellinger, 1991). Note that, in some cases, where only 2D cuts of the wavefield are considered, it may still make sense to use notations of P, SV, and SH even though they might be misleading. For example, in the symmetry planes of orthorhombic media where the point singularities can potentially happen, these notations are acceptable because the polarization vectors behave as if they follow the analogous intersection singularity in TI media.

Dellinger (1991) showed that sorting the modes based on the magnitude of the phase velocity involves the problem of particle-motion discontinuity at the S-wave

singularities, and therefore, does not lead to a clear separation. In the Fourier domain, this local discontinuity behaves similarly to a delta function and generates a strong planar artifact in the space domain. A similar artifact can be seen when S-wave modes with intersection singularity are being separated in 2D TI media based on their phase velocities. In the case of TI media, this planar artifact can be eliminated because of the use of SV and SH definitions that ensure polarization continuity in all phase directions. However, as described above, the same approach is not applicable in the case of low-symmetry anisotropic media. In order to successfully separate the wavefields of S-wave modes in such media, it is necessary to address the discontinuity problem.

In this paper, for the analysis on the S-wave polarization vectors and singularities (Figures 1-6), we adopt an example of orthorhombic medium from Schoenberg and Helbig (1997), which has the following density-normalized stiffness coefficients (in km^2/s^2):

$$c_{ij} = \begin{bmatrix} 9 & 3.6 & 2.25 & 0 & 0 & 0 \\ 3.6 & 9.84 & 2.4 & 0 & 0 & 0 \\ 2.25 & 2.4 & 5.9375 & 0 & 0 & 0 \\ 0 & 0 & 0 & 2 & 0 & 0 \\ 0 & 0 & 0 & 0 & 1.6 & 0 \\ 0 & 0 & 0 & 0 & 0 & 2.182 \end{bmatrix}. \tag{19}$$

For the triclinic example, we use the stiffnesses given by Mah and Schmitt (2003):

$$c_{ij} = \begin{bmatrix} 14.9 & 6.3 & 5.2 & 0.7 & 0.9 & -0.5 \\ 6.3 & 14.9 & 5.7 & 0.8 & 1.5 & -0.4 \\ 5.2 & 5.7 & 10.0 & 0.7 & 0.8 & 0.1 \\ 0.7 & 0.8 & 0.7 & 3.3 & -0.1 & 0.1 \\ 0.9 & 1.5 & 0.8 & -0.1 & 3.0 & 0.2 \\ -0.5 & -0.4 & 0.1 & 0.1 & 0.2 & 3.7 \end{bmatrix}. \tag{20}$$

LOCATING SINGULARITIES

Crampin (1984, 1991) showed that kiss and point singularities are the only possible kinds of singularity in orthorhombic or any other lower-symmetry media. In order to get rid of the planar artifacts caused by polarization discontinuity at such locations, we need first to locate the singularities. Locations of singularities correspond to the locations where the Christoffel matrix **G** degenerates and the phase velocities of both S waves become equal. In low-symmetry anisotropic media, S waves have the following well-known explicit expressions for phase velocity (Schoenberg and Helbig,
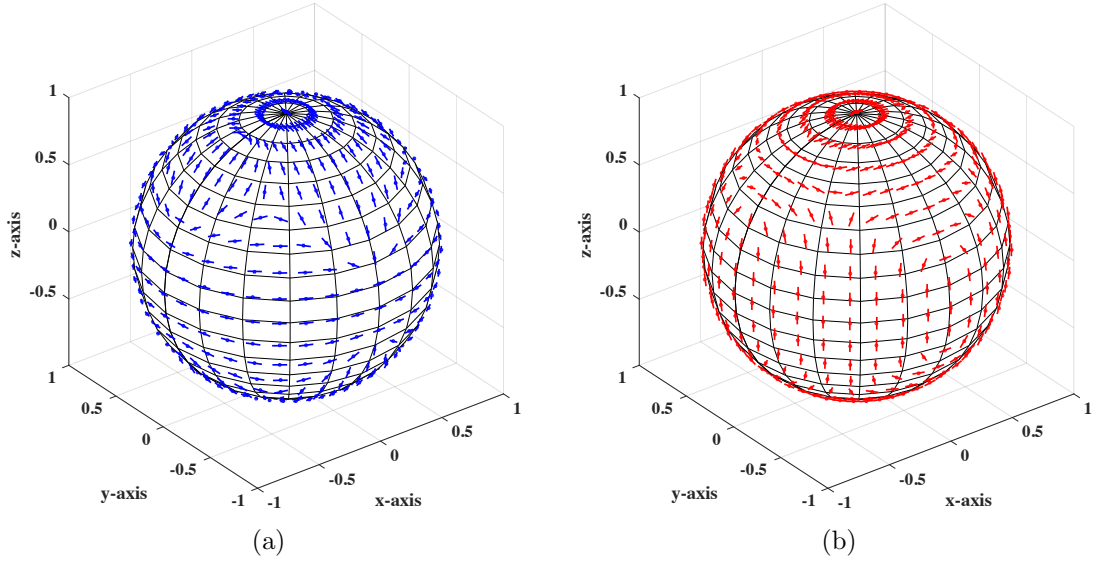
Figure 1: Polarization vectors of a) S1 (blue) and b) S2 (red) modes in the orthorhombic model (equation 19) plotted on a unit sphere. Notice the sudden polarization vectors flip in the $[x, z]$ and $[y, z]$ planes and in the plane along $x = y$. These effects are observed as these planes cut through point singularities and they resemble jumping between modes at the intersection singularity.
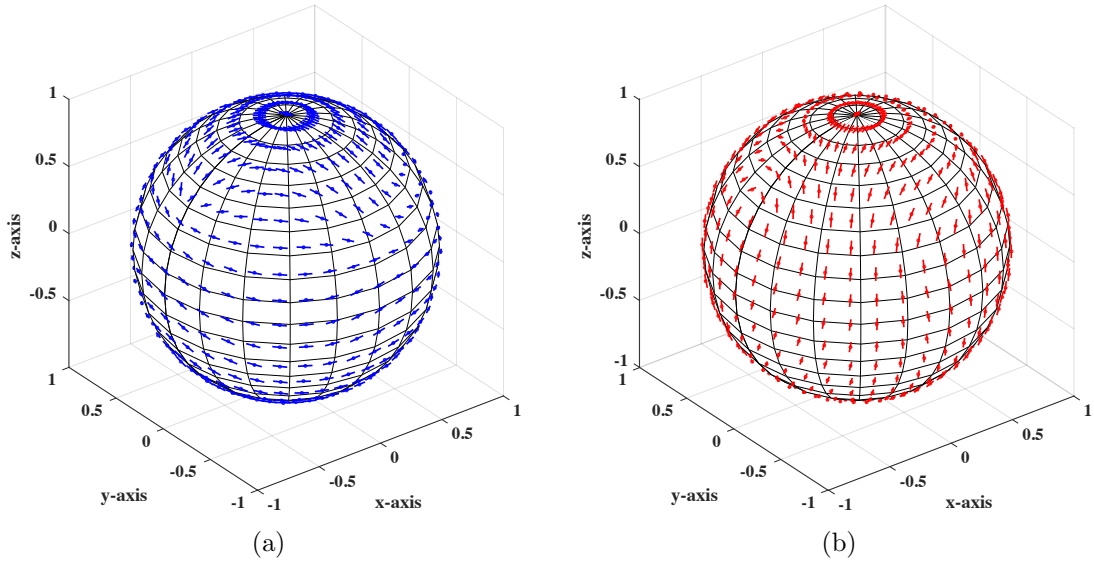

Figure 2: Polarization vectors of a) S1 (blue) and b) S2 (red) modes in the triclinic model (equation 20) plotted on a unit sphere. Notice the patternless variation of polarizations with respect to phase directions due to the presence of only point symmetry.

1997; Tsvankin, 1997, 2012):

$$v_{S1}^2(c_{ij}, \mathbf{n}) = 2\sqrt{\frac{-d}{3}}\cos(\frac{\nu}{3} + \frac{2\pi}{3}) - \frac{a}{3} , \tag{21}$$

$$v_{S2}^2(c_{ij}, \mathbf{n}) = 2\sqrt{\frac{-d}{3}}\cos(\frac{\nu}{3} + \frac{4\pi}{3}) - \frac{a}{3} , \tag{22}$$

where

$$\nu\ (c_{ij}, \mathbf{n}) = \arccos\left(\frac{-q}{2\sqrt{(-d/3)^3}}\right) ,$$

$$q\ (c_{ij}, \mathbf{n}) = 2\left(\frac{a}{3}\right)^3 - \frac{ab}{3} + c , \quad d = -\frac{a^2}{3} + b ,$$

$$a\ (c_{ij}, \mathbf{n}) = -(G_{11} + G_{22} + G_{33}) ,$$

$$b\ (c_{ij}, \mathbf{n}) = G_{11}G_{22} + G_{11}G_{33} + G_{22}G_{33} - G_{12}^2 - G_{13}^2 - G_{23}^2 ,$$

$$c\ (c_{ij}, \mathbf{n}) = G_{11}G_{23}^2 + G_{22}G_{13}^2 + G_{33}G_{12}^2 - G_{11}G_{22}G_{33} - 2G_{12}G_{13}G_{23} .$$

G_{ij} are given in equation A-2 for the most general case of triclinic media and are functions of local stiffness c_{ij} and phase direction $\mathbf{n} = \bar{\mathbf{k}} = \mathbf{k}/|\mathbf{k}|$. Equations 21 and 22 can be derived from the generic solution of a cubic equation for v^2, which corresponds to the Christoffel equation. They are valid for any locally homogeneous anisotropic medium with associated G_{ij} (Schoenberg and Helbig, 1997). With these analytical expressions, we can derive the sufficient condition for the occurence of a S-wave singularity. From $v_{S1}^2 = v_{S2}^2$ and equations 21 and 22, it follows that in the singular direction $\hat{\mathbf{n}}$,

$$\cos(\frac{\nu\ (c_{ij}, \hat{\mathbf{n}})}{3} + \frac{2\pi}{3}) = \cos(\frac{\nu\ (c_{ij}, \hat{\mathbf{n}})}{3} + \frac{4\pi}{3}) , \tag{23}$$

or doing trigonometric expansions,

$$\cos(\frac{\nu\ (c_{ij}, \hat{\mathbf{n}})}{3})\cos(\frac{2\pi}{3}) - \sin(\frac{\nu\ (c_{ij}, \hat{\mathbf{n}})}{3})\sin(\frac{2\pi}{3}) = \cos(\frac{\nu\ (c_{ij}, \hat{\mathbf{n}})}{3})\cos(\frac{4\pi}{3}) - \sin(\frac{\nu\ (c_{ij}, \hat{\mathbf{n}})}{3})\sin(\frac{4\pi}{3}) , \tag{24}$$

which leads to the condition of

$$\sin\left(\frac{\nu\ (c_{ij}, \hat{\mathbf{n}})}{3}\right) = 0 . \tag{25}$$

We propose to apply equation 25 to numerically detect the proximity of the point singularity for a given phase direction. This condition also allows us to create a filter with an adjustable effective area to smooth the polarization vectors around the singularity in order to attenuate the planar artifacts in wave-mode separation and wave vector decomposition. The variation of values of the left-hand side in equation 25 with different phase directions ($\mathbf{n}$) in the case of the example orthorhombic model is shown in Figure 3b. Similar plots for the triclinic model are shown in Figures 4 and 5.
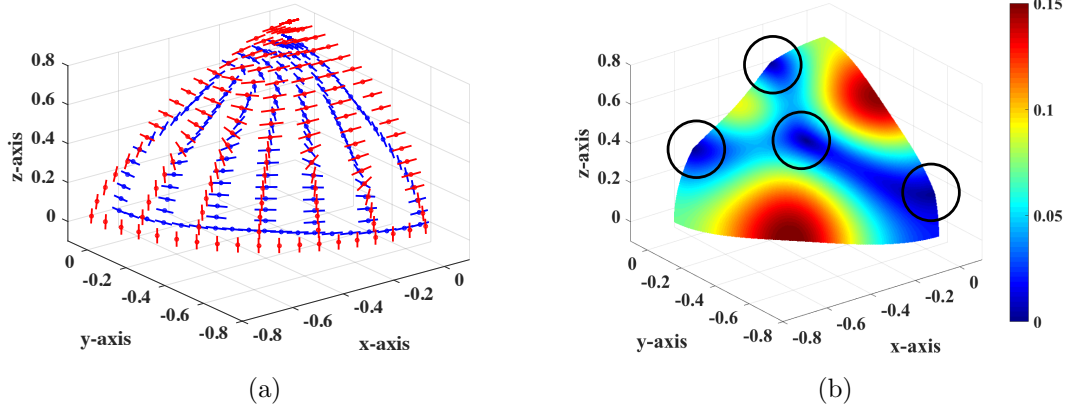
Figure 3: a) Polarization vectors in the orthorhombic model of S1 (blue) and S2 (red) plotted on phase slowness surfaces to show how they rapidly rotate in the vicinity of point singularities. b) $\sin\left(\nu\left(c_{ij}, \mathbf{n}\right)/3\right)$ for different phase directions ($\mathbf{n}$) plotted on S1 phase slowness surface. Notice that the values turn zero at the locations corresponding to point singularities in circles and that there are two point singularities in the $[x, z]$ plane, one in $[y, z]$ planes, and one in the plane cut along $x = y$ in this octant.

NUMERICAL ALGORITHM

We can summarize the steps of the proposed elastic wave-vector decomposition as follows:

1. Considering the decomposition operator given in equation 14, we define each component of the decomposed wavefield corresponding to α wave mode as

$$
\begin{aligned}
\widetilde{U}_x^\alpha &= A_{xx}^\alpha \widetilde{U}_x + A_{xy}^\alpha \widetilde{U}_y + A_{xz}^\alpha \widetilde{U}_z \ , \\
\widetilde{U}_y^\alpha &= A_{yy}^\alpha \widetilde{U}_y + A_{xy}^\alpha \widetilde{U}_x + A_{yz}^\alpha \widetilde{U}_z \ , \\
\widetilde{U}_z^\alpha &= A_{zz}^\alpha \widetilde{U}_z + A_{xz}^\alpha \widetilde{U}_x + A_{yz}^\alpha \widetilde{U}_y \ ,
\end{aligned}
\tag{26}
$$

   where each A_{ij}^α with i and j denoting different components x, y, and z is given in equation 16.

2. To implement the proposed filtering of singularities, we multiply each component by a weighting factor defined as

$$
\hat{A}_{ij}^\alpha = A_{ij}^\alpha \ w(\nu, \tau) \ ,
\tag{27}
$$

   where $w(\nu, \tau) = \min\left(\frac{\sin(\frac{\nu}{3})}{\tau}, 1\right)$, $\hat{A}_{ij}^\alpha$ denotes the modified version of A_{ij}^α, which is used in equation 26, and τ is a thresholding parameter. This filtering process results in small $\hat{A}_{ij}^\alpha$ in places where the given phase direction $\mathbf{n}$ is close to the direction of a singularity. Figure 6 shows how the weight $w(\nu, \tau)$ changes with respect to different values of τ in the case of the example orthorhombic model.
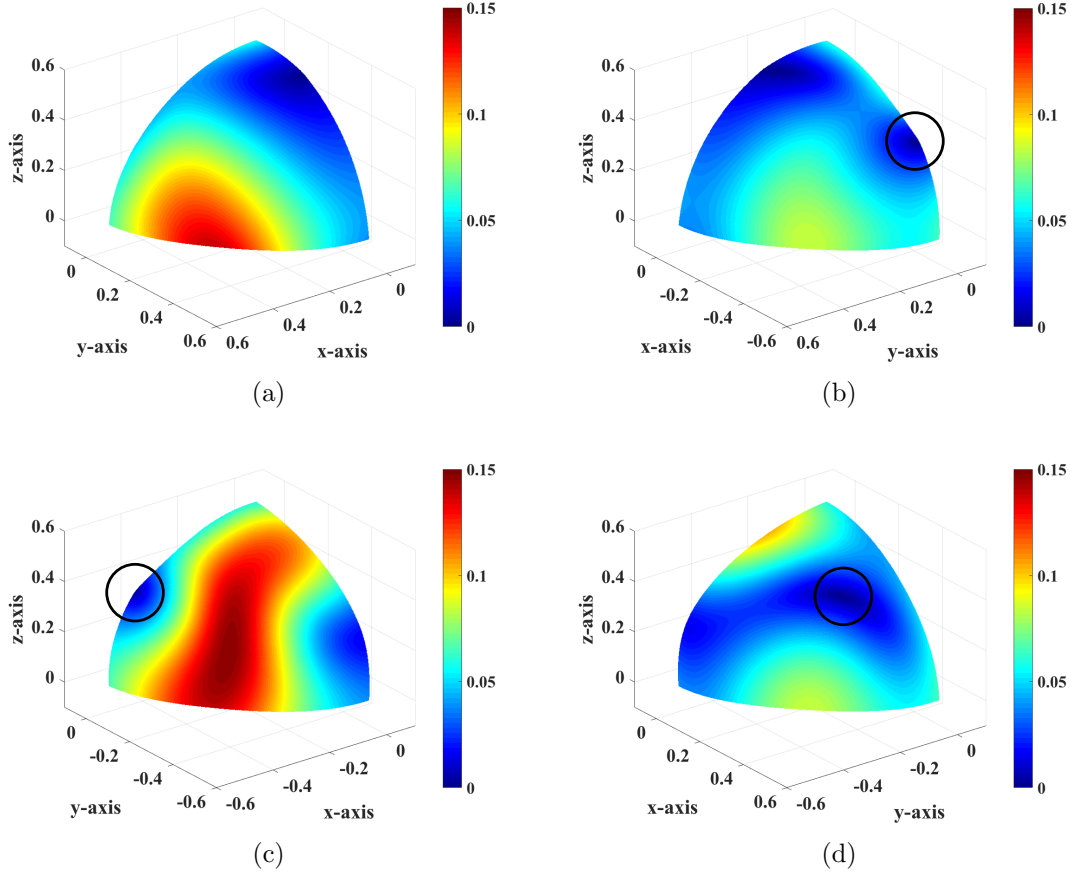
Figure 4: $\sin\left(\nu\left(c_{ij}, \mathbf{n}\right)/3\right)$ for different phase directions ($\mathbf{n}$) plotted on S1 phase slowness surface the zenith angle $\theta = 0° - 90°$ measured from vertical and from the azimuthal angle a) $\phi = 0° - 90°$, b) $\phi = 90° - 180°$, c) $\phi = 180° - 270°$, and d) $\phi = 270° - 360°$ measured with respect to x-axis. Notice that the values turn zero at the locations corresponding to singularities in circles.
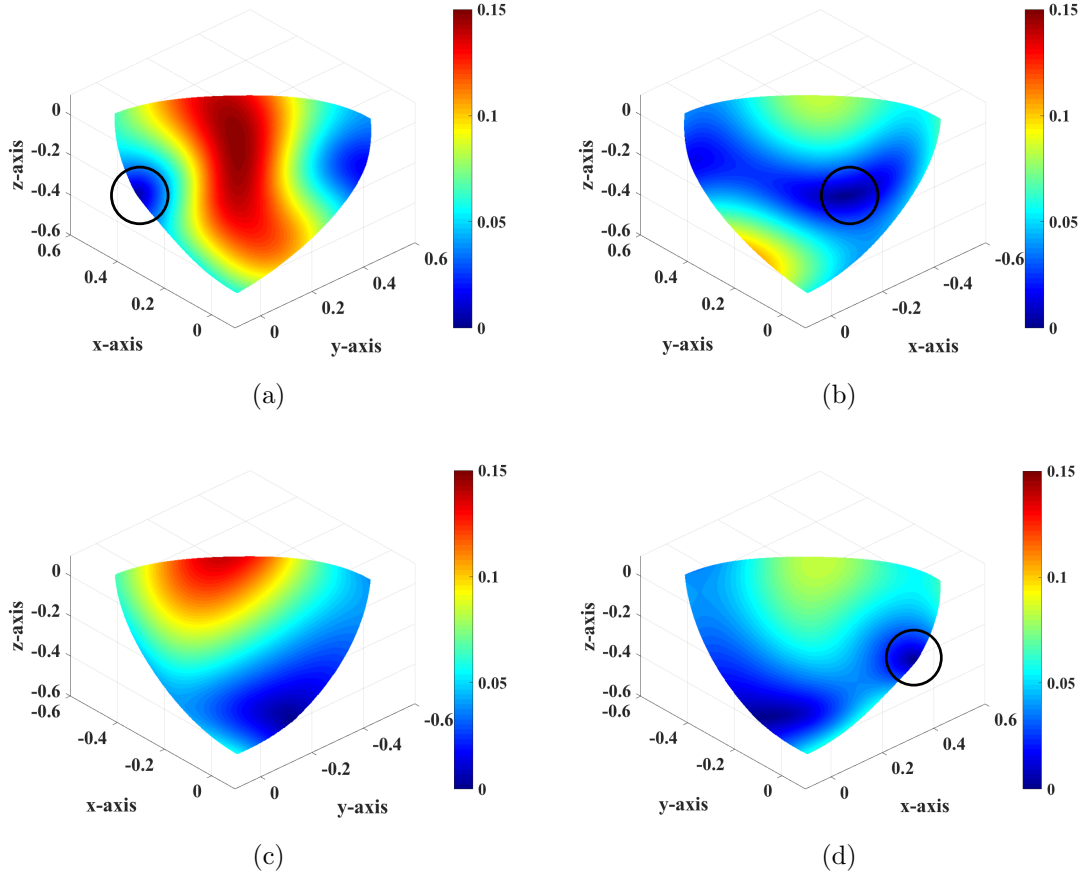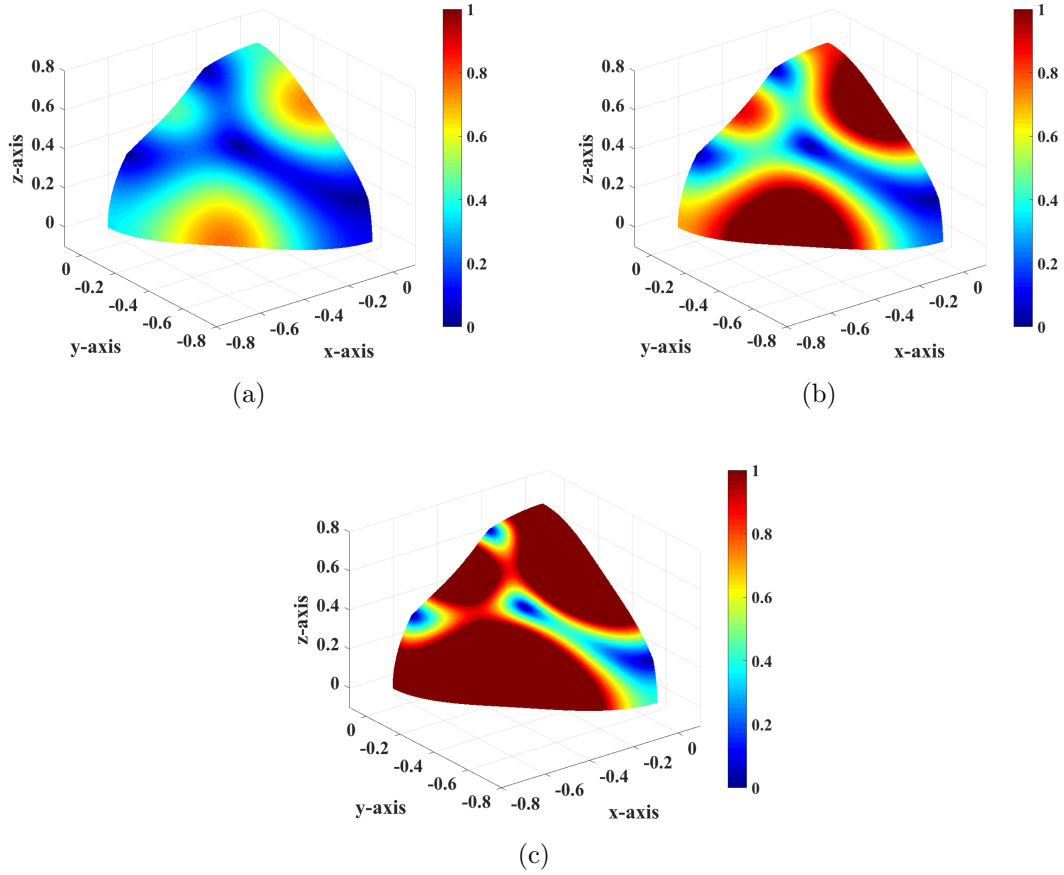
Figure 5: $\sin\left(\nu\ (c_{ij}, \mathbf{n})/3\right)$ for different phase directions ($\mathbf{n}$) plotted on S1 phase slowness surface the zenith angle $\theta = 90° - 180°$ measured from vertical and from the azimuthal angle a) $\phi = 0° - 90°$, b) $\phi = 90° - 180°$, c) $\phi = 180° - 270°$, and d) $\phi = 270° - 360°$ measured with respect to x-axis. Notice that the values turn zero at the locations corresponding to singularities in circles.

(a)

(b)

(c)

Figure 6: Weight $w(\nu, \tau)$ in equation 27 with a) $\tau = 0.2$, b) $\tau = 0.1$, and c) $\tau = 0.05$ for the case of the example orthorhombic model.

3. We then implement equation 26 with modified coefficients according to equation 27 applying the low-rank approximation as formulated in equation 18.

4. As the last step, we compensate for the lost in amplitude information from the previous smoothing step using local signal-noise orthogonalization (Chen and Fomel, 2015) as described by

$$\mathbf{U}^{\alpha}(\mathbf{x}) = \left(1 + \left\langle \frac{\mathbf{U}_0^{\alpha}(\mathbf{x}) - \mathbf{U}_{\tau}^{\alpha}(\mathbf{x})}{\mathbf{U}_{\tau}^{\alpha}(\mathbf{x})} \right\rangle \right) \mathbf{U}_{\tau}^{\alpha}(\mathbf{x}) \,, \tag{28}$$

where $\mathbf{U}_0^{\alpha}(\mathbf{x})$ and $\mathbf{U}_{\tau}^{\alpha}(\mathbf{x})$ denote the separated wavefield without smoothing ($\tau = 0$) and with the specified smoothing respectively. $\mathbf{U}^{\alpha}(\mathbf{x})$ denotes the final separated wavefield after amplitude compensation and $\langle \cdot \rangle$ represents a smooth division operator. The notion behind equation 28 is that the desired signal ($\mathbf{U}_{\tau}^{\alpha}(\mathbf{x})$) is assumed to be locally orthogonal to the noise ($\mathbf{U}_0^{\alpha}(\mathbf{x}) - \mathbf{U}_{\tau}^{\alpha}(\mathbf{x})$). Therefore, we can extract the remaining part of the signal in the noise—the missing amplitudes from the smoothing process—and simply add it back for the signal reconstruction.

EXAMPLES

Homogeneous orthorhombic model

To test the proposed method, we first use the standard model in equation 19 (Schoenberg and Helbig, 1997) and assume that the planes of symmetry coincide with the coordinate planes. A point displacement source with equal magnitude in all components is used. The full elastic wavefield is generated using a low-rank one-step elastic wave propagator (Sun et al., 2016b,a) from the source, which is located in the middle of the model. The wave snapshot is shown in Figure 7 at time $0.15 \, s$. We decompose the wavefield according to the steps described in the previous section. Figure 8 shows P wave mode separated from the original wavefield, which appears clean with no visible artifacts. For conciseness, we show only the y-component of the separated S1 and S2 wavefields in Figures 9 and 10. Note that setting the smoothing parameter $\tau = 0$ is equivalent to not applying any weighting to the A_{ij}^{α} (equation 27). We observe reduced planar artifacts in comparison of results from before and after the implementation of the proposed smoothing method (Figures 9b and 10b). We subsequently supply the results from this step to the amplitude compensation process (equation 28). The y-component of the separated wavefields with and without corrected amplitudes is shown in comparison in Figures 9c and 10c that use the same clipping. We observe clean separated wavefields with no apparent artifacts and corrected amplitudes close to those in the original wavefields in Figures 9a and 10a.
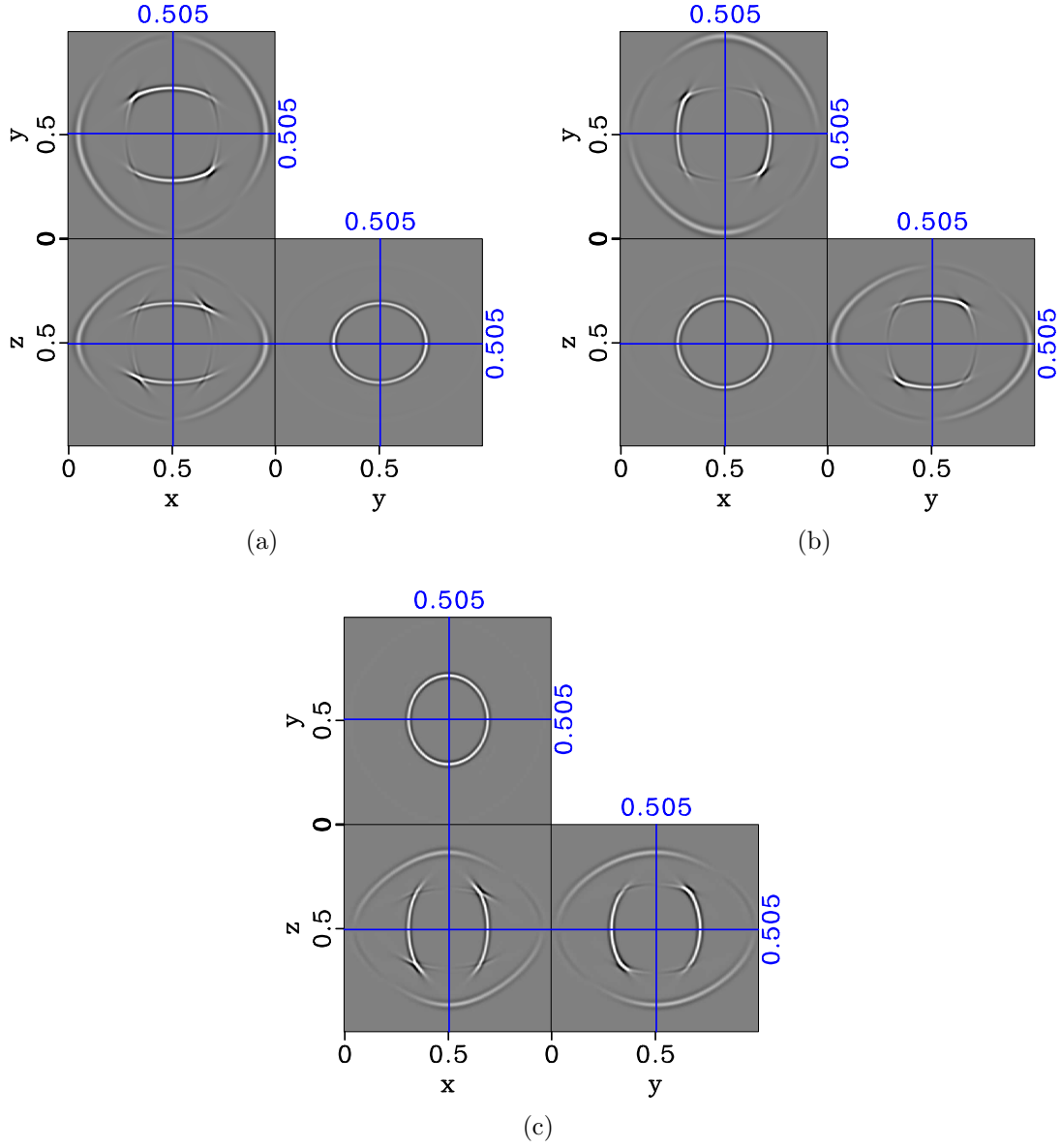
(a)

(b)

(c)

Figure 7: Original elastic wavefield in $[x, z]$, $[y, z]$, and $[x, y]$ planes generated from the stiffness tensor coefficients of the orthorhombic model (equation 19) a) x-component b) y-component c) z-component.
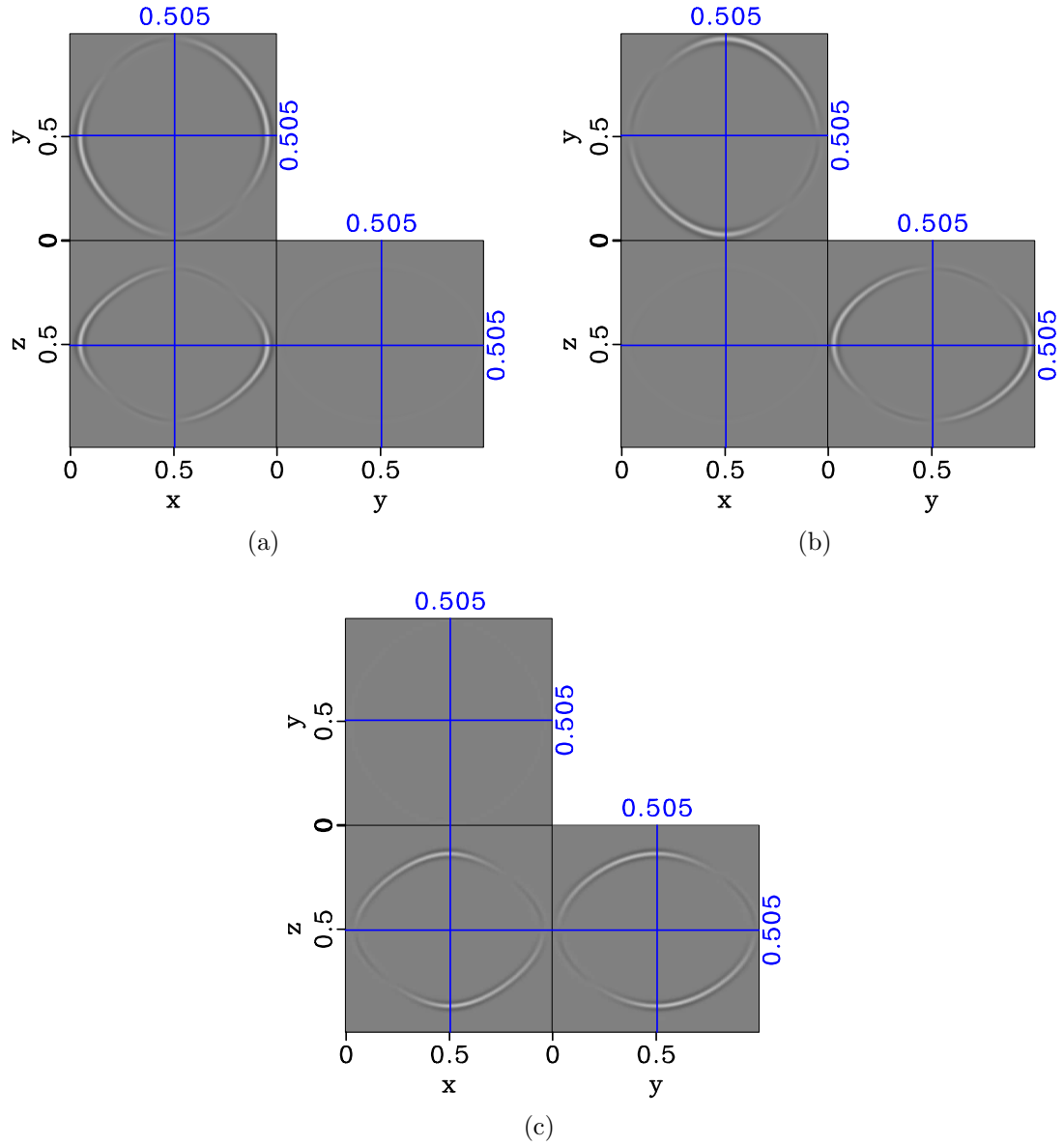
Figure 8: Components of a P elastic wavefield from a point displacement source in the orthorhombic model (equation 19) a) x-component b) y-component c) z-component.
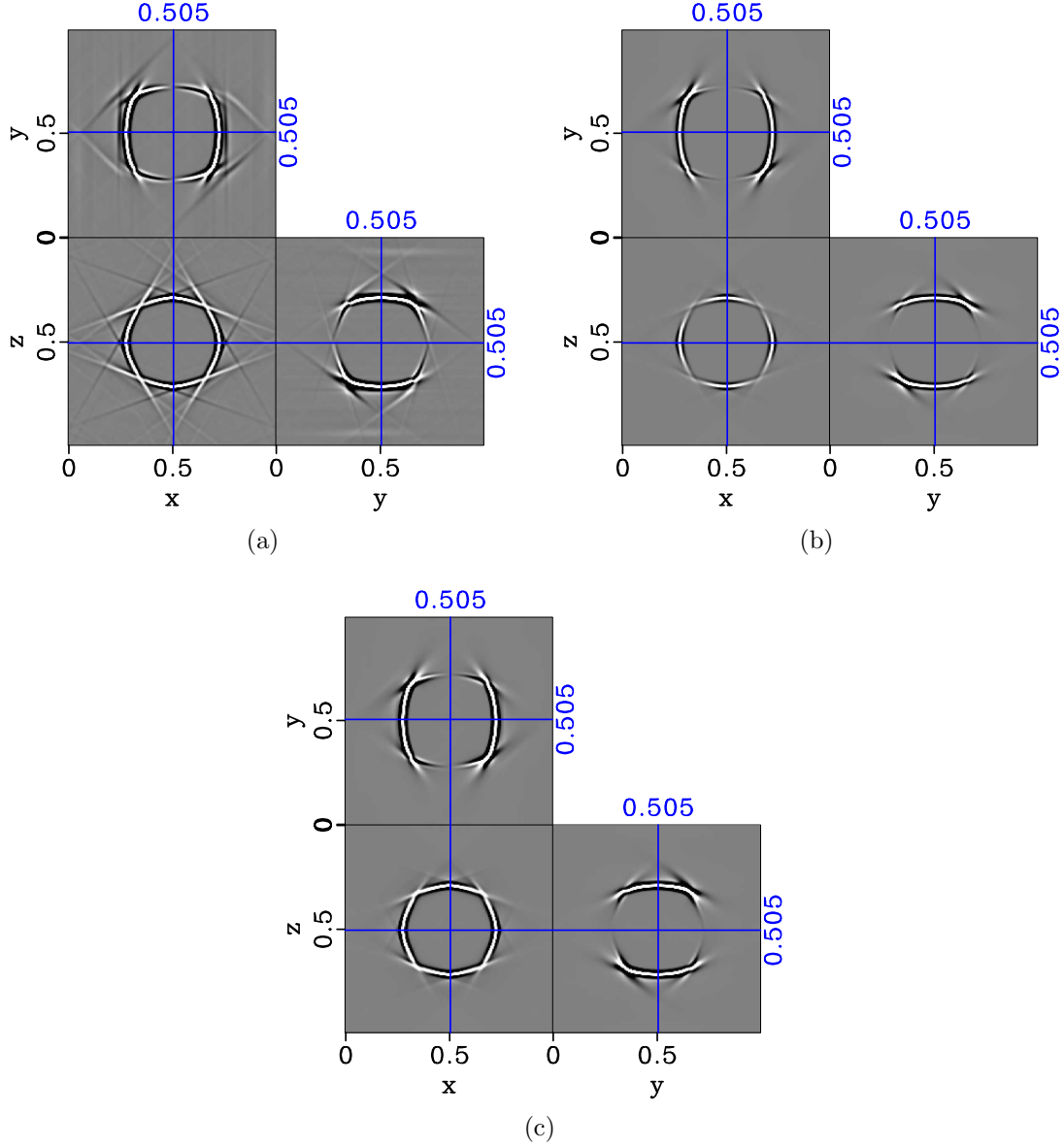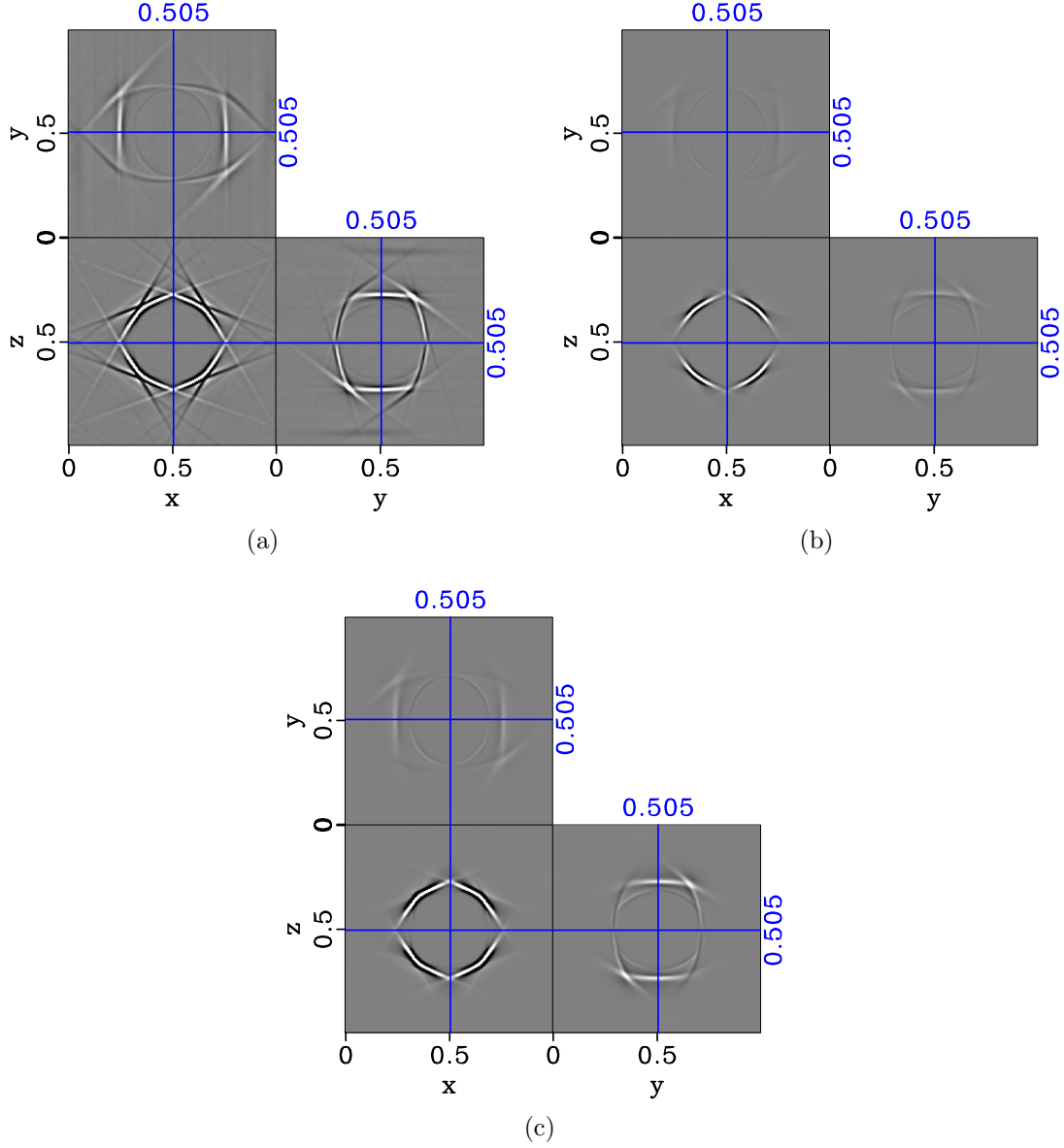
Figure 9: Separated y-component of S1 elastic wavefield in the orthorhombic model (equation 19) with τ equal to a) 0 (no smoothing) b) 0.2. The final seprated wavefield with amplitude compensation (equation 28) is shown in c). Notice planar artifacts disappearing when the proposed smoothing filter is applied as shown in b) and with the restored amplitude as shown in c). The clipping has been adjusted to enhance visualization and stay constant in all three plots.

(a)

(b)

(c)

Figure 10: Separated y-component of S2 elastic wavefield in the orthorhombic model (equation 19) with τ equal to a) 0 (no smoothing) b) 0.2. The final seprated wavefield with amplitude compensation (equation 28) is shown in c). Notice planar artifacts disappearing when the proposed smoothing filter is applied as shown in b) and with the restored amplitude as shown in c). The clipping has been adjusted to enhance visualization and stay constant in all three plots.

Homogeneous triclinic model

To further test the proposed method in a low-symmetry anisotropic model, we use next a triclinic model with parameters specified in equation 20. Similar to before, a point displacement source with equal magnitude in all components is used. The full elastic wavefield is generated in the same manner and shown in Figure 11 at time 0.13 *s*. We observe a complicated behavior of the two S-wave modes in comparison with the orthorhombic case in Figure 7. We show only the y-component of the separated S1 and S2 wavefields in Figures 12 and 13 for conciseness. We observe reduced planar artifacts after the implementation of the proposed smoothing method and further correct the amplitudes. The y-component of the resultant separated wavefields with and without corrected amplitudes are shown in comparison in Figure 12. We observe again clean separated wavefields with no apparent artifacts and correct amplitudes similar to the previous case of homogeneous orthorhombic model.

Two-layered heterogeneous triclinic model

For our final test, we consider the two-layered French model (French, 1974) where the interface is made of various geometrical shapes. The model c_{ij} parameters of both sublayers are heterogeneous and changing vertically as

$$c_{ij} = c_{ij}^0 \left(1 + \beta(z - z_0) \right) , \qquad (29)$$

where c_{ij}^0 denotes the value of stiffness at the reference depth z_0, β is the gradient, and c_{ij} represents the value at other depths. For the top layer, c_{ij}^0 is 0.75 times the stiffnesses of the tricnic model (equation 20), $\beta = 0.6375$,and $z_0 = 0.4$ *km*. For the bootm layer, c_{ij}^0 is equal to the stiffnesses of the tricnic model (equation 20), $\beta = 0.425$, and $z_0 = 0.8$ *km*. Figure 14 shows the plot of the density normalized c_{11} in this setting. Other stiffnesses have similar appearance but with different values. A time snapshot at time 0.12 *s* of the full elastic wavefield is shown in Figure 15. We use the same oriented source as in the previous cases and put it at the middle of the model. Figures 16 and 17 show the resultant y-component of separated S1 and S2 wavefields. The final results with corrected amplitudes are shown in Figures 16c and 17c. Similar conclusions can be drawn as in the previous cases.

DISCUSSION

The proposed wave-vector decomposition method utilizes an analytical expression for locating singularities (equation 25) as the basis for a non-stationary smoothing operator (equation 27) defined as a weighting in the wavenumber domain. The analytical expression is a function of the components of the Christoffel matrix **G** variable in space and phase directions defined by the wavenumbers. Because the S-wave phase
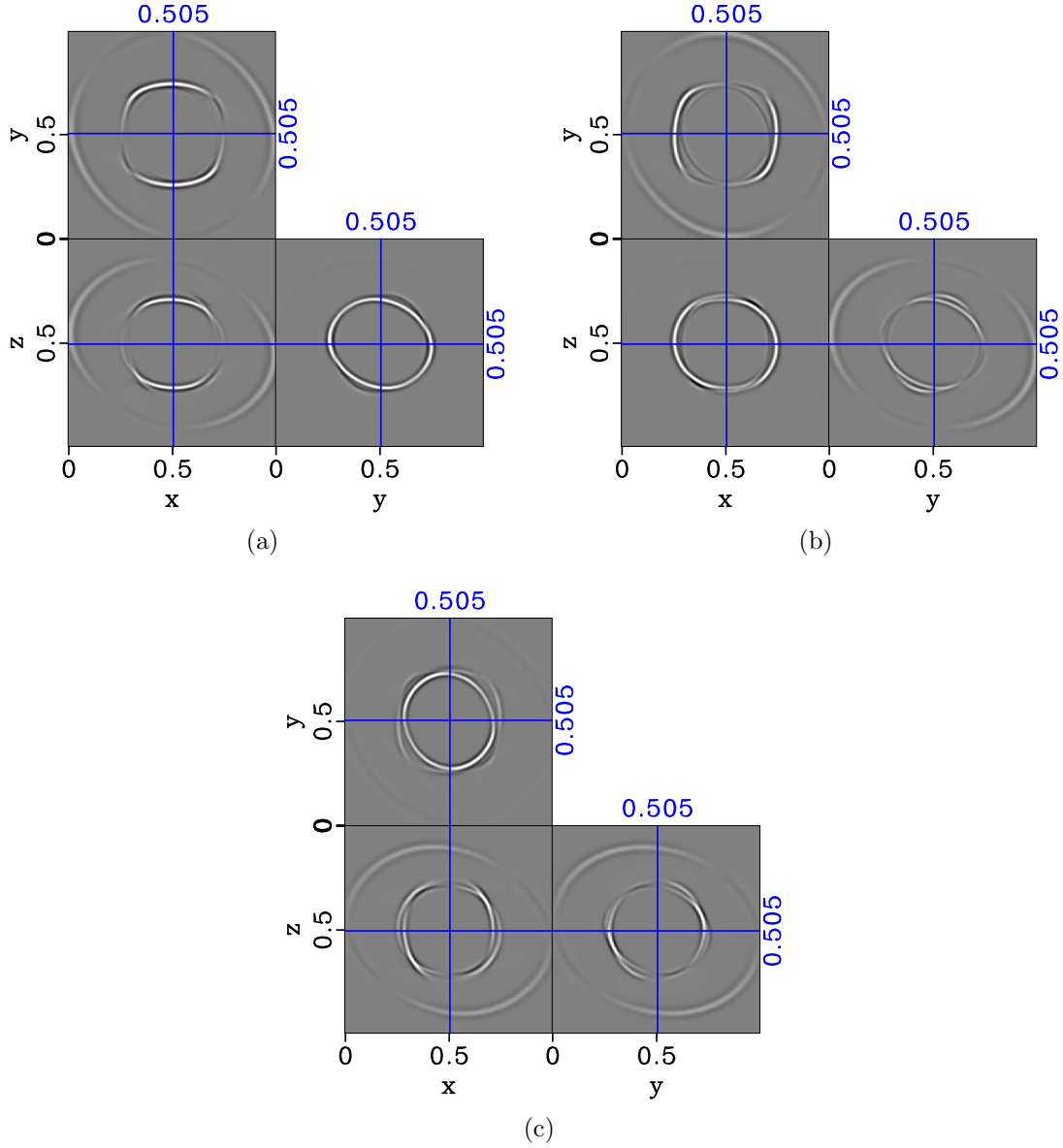
Figure 11: Original elastic wavefield in $[x, z]$, $[y, z]$, and $[x, y]$ planes generated from the stiffness tensor coefficients of the triclinic model (equation 20) a) x-component b) y-component c) z-component. One can observe more complicated S-wave behaviors that those in the orthorhombic model (Figure 7).
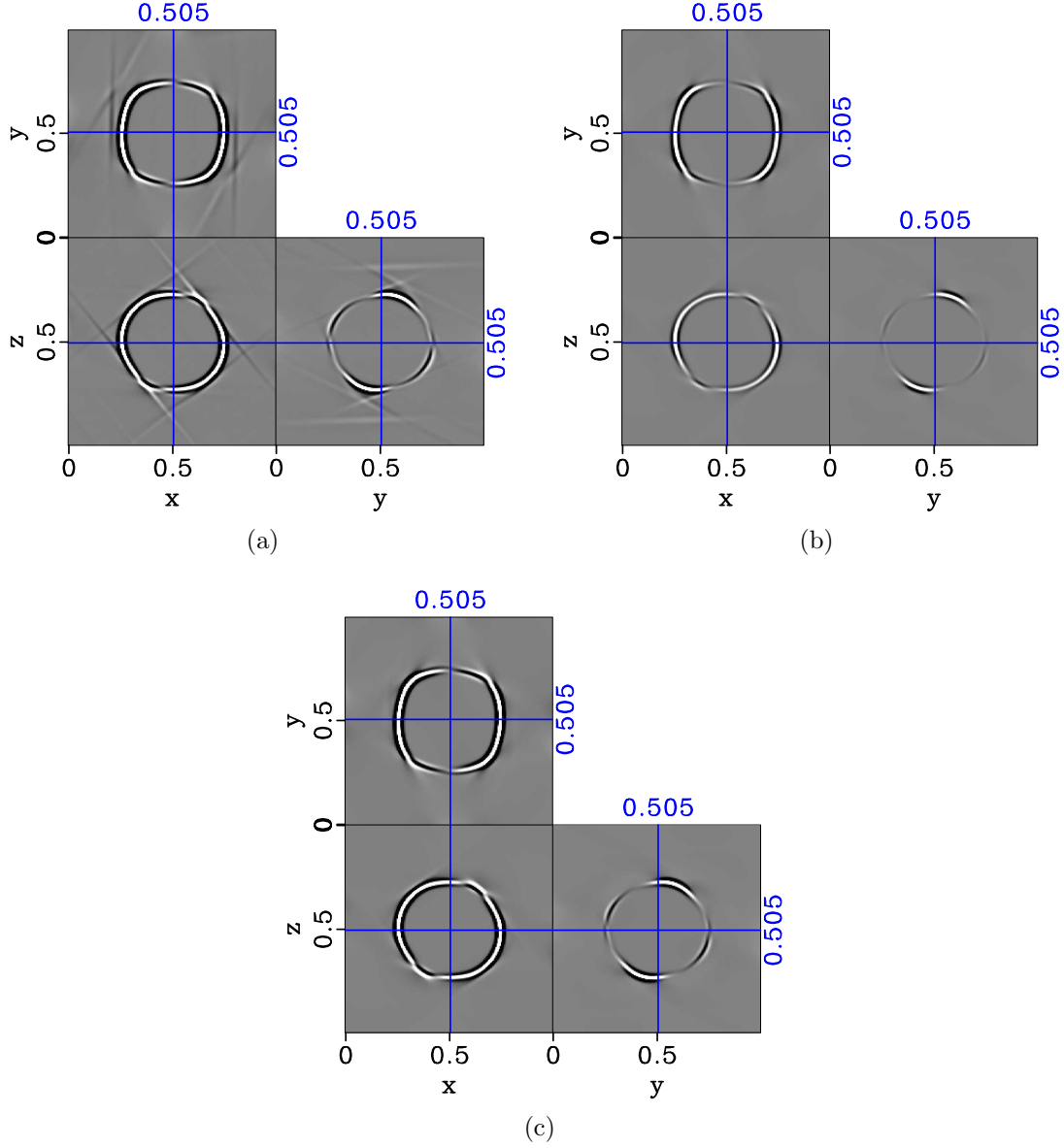
Figure 12: Separated y-component of S1 elastic wavefield in the triclinic model (equation 20) with τ equal to a) 0 (no smoothing) b) 0.2. The final seprated wavefield with amplitude compensation (equation 28) is shown in c). Notice planar artifacts disappearing when the proposed smoothing filter is applied as shown in b) and with the restored amplitude as shown in c). The clipping has been adjusted to enhance visualization and stay constant in all three plots.
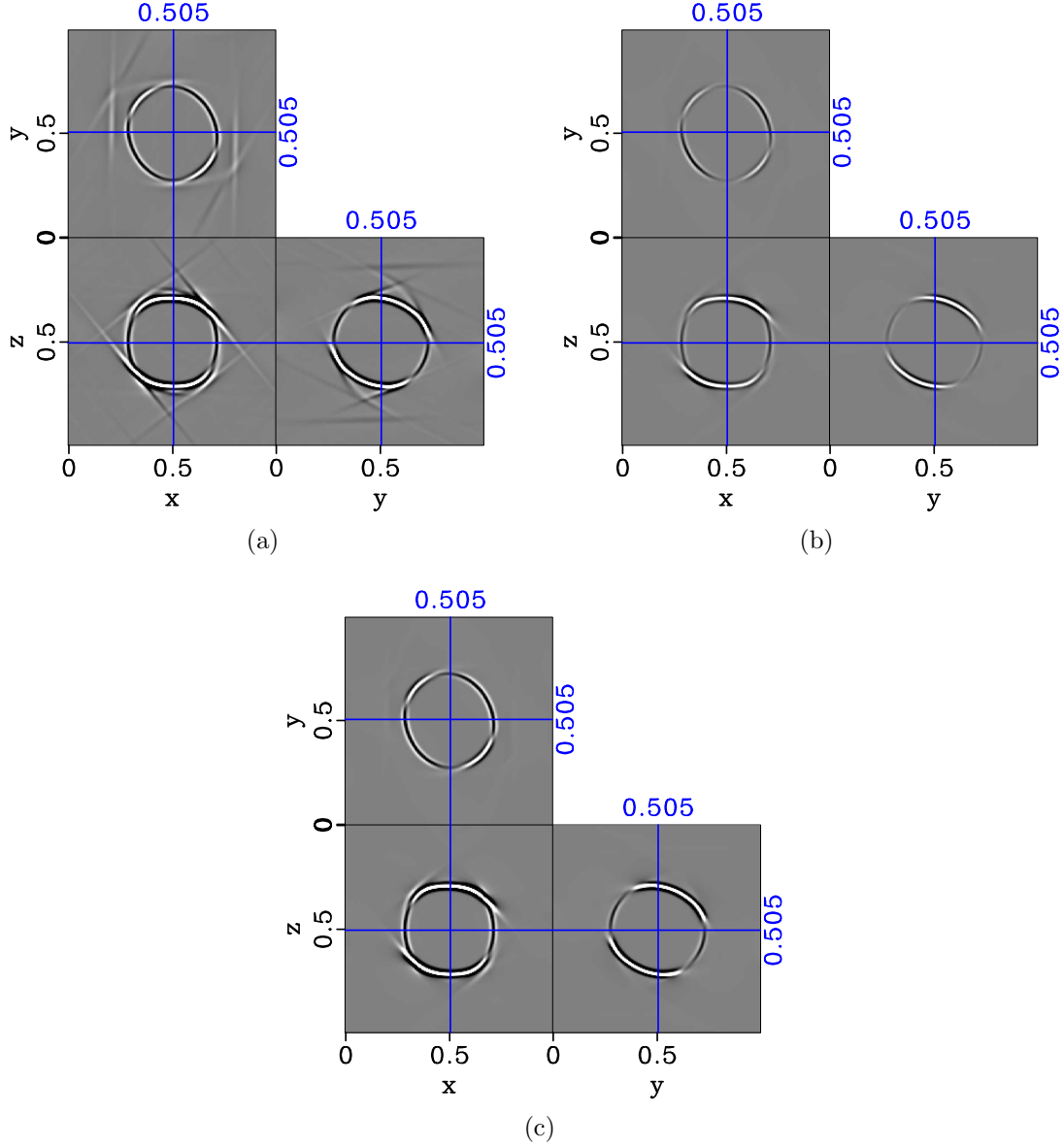
Figure 13: Separated y-component of S2 elastic wavefield in the triclinic model (equation 20) with τ equal to a) 0 (no smoothing) b) 0.2. The final seprated wavefield with amplitude compensation (equation 28) is shown in c). Notice planar artifacts disappearing when the proposed smoothing filter is applied as shown in b) and with the restored amplitude as shown in c). The clipping has been adjusted to enhance visualization and stay constant in all three plots.
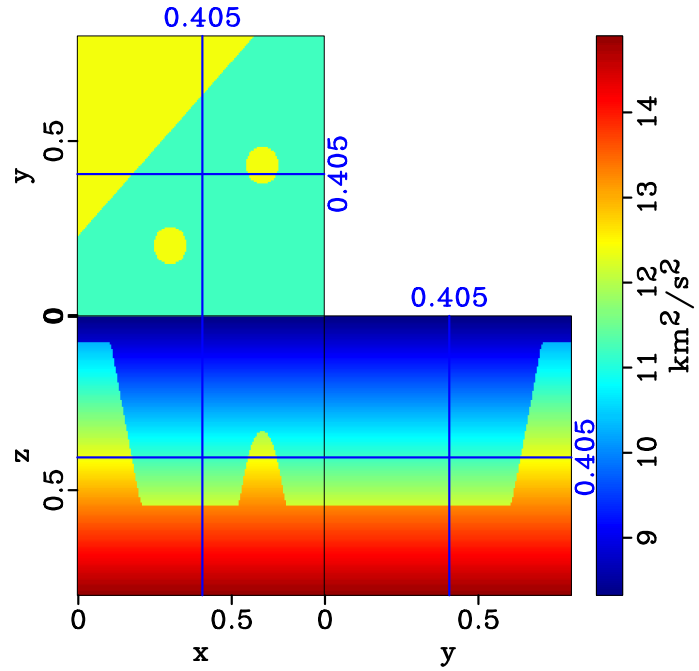
Figure 14: Density normalized c_{11} for the two-layered heterogeneous triclinic model. The parmeters are subjected to the heterogeneity specified in equation 29.

velocities in low-symmetry media (including orthorhombic, monoclinic, and triclinic) can be computed based on the same generic formulas (equations 21 and 22) with a corresponding change in **G**, the same analytical condition for locating singularities can also be used in those media. In this paper, we have demonstrated the applicability of the proposed method for wave-vector decomposition in low-symmetry anisotropic media using synthetic examples with orthorhombic and triclinic symmetries.

Alternatively to solving the Christoffel equation numerically for exact values of polarizations, one may choose to use an analytical approximation in weakly anisotropic media derived from perturbation theory (Farra and Pšenčík, 2003). This choice may lead to increased computational efficiency in complex models.

Generally, the knowledge of polarization vectors and their applicability are based on the underlying assumption in which the medium is assumed to be locally homogeneous relative to the propagating frequency of the waves. In the case of a larger degree of heterogeneity such as strong contrasts and considerable velocity gradients, this assumption is approximate and may need special care.

To implement wave-vector decomposition, the proposed method uses the low-rank approximations for the decomposition operator (equation 12). This allows us to avoid explicitly computing and storing the polarizations of the mode of interest at every grid point, which would be prohibitively expensive. The proposed method is appropriate for decomposing the elastic wavefields during the backward propagation step in elastic reverse-time migration (RTM) (Wang et al., 2016) and full-waveform inversion (FWI) (Wang et al., 2015). We did not consider the problem of separating wave modes in recorded surface seismic data.
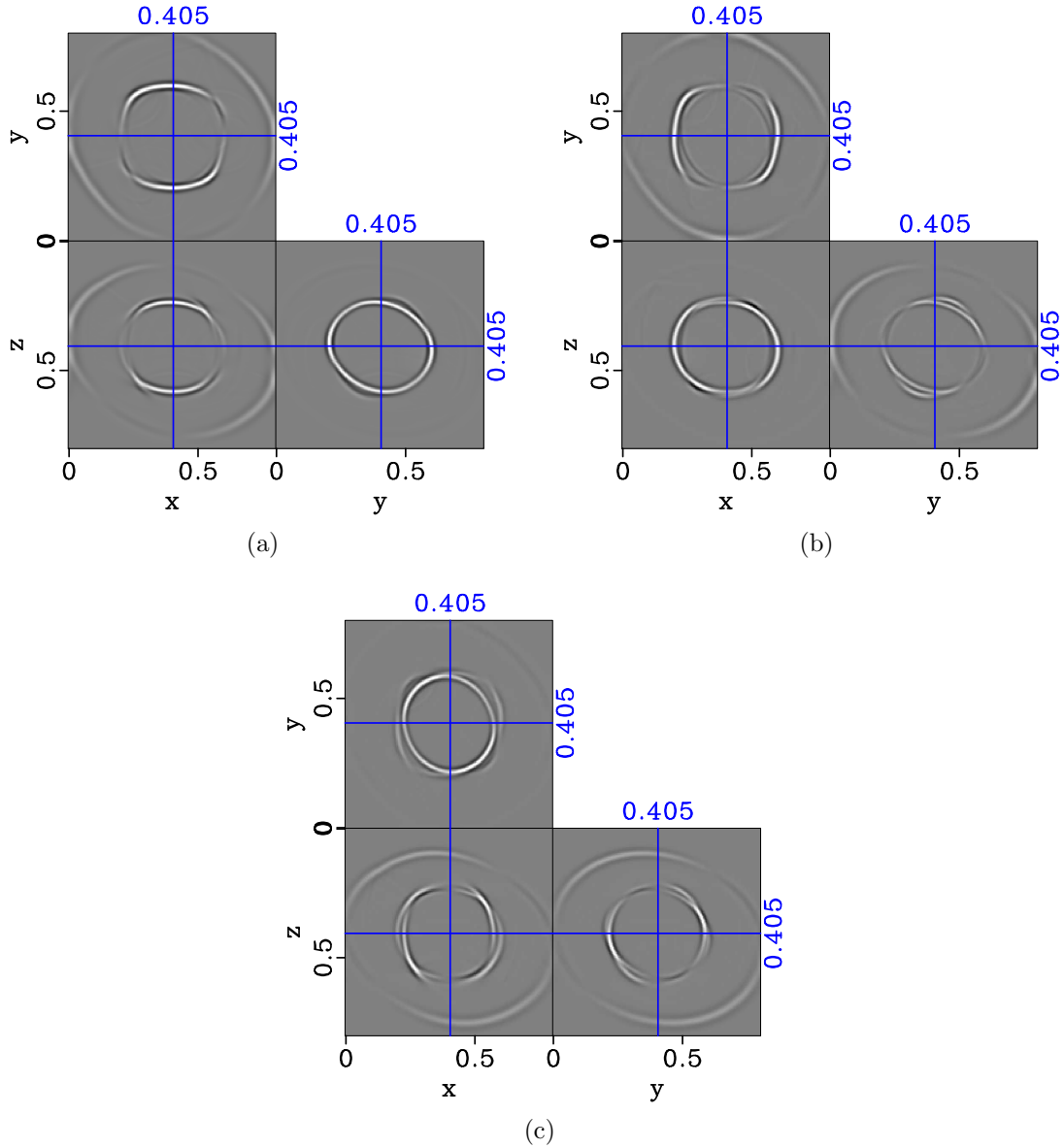
Figure 15: Original elastic wavefield in $[x, z]$, $[y, z]$, and $[x, y]$ planes generated from the stiffness tensor coefficients of the two-layered heterogenous triclinic model (equation 29) a) x-component b) y-component c) z-component. One can observe more complicated S-wave behaviors that those in the homogeneous orthorhombic model (Figure 7) and homogeneous triclinic model (Figure 15).
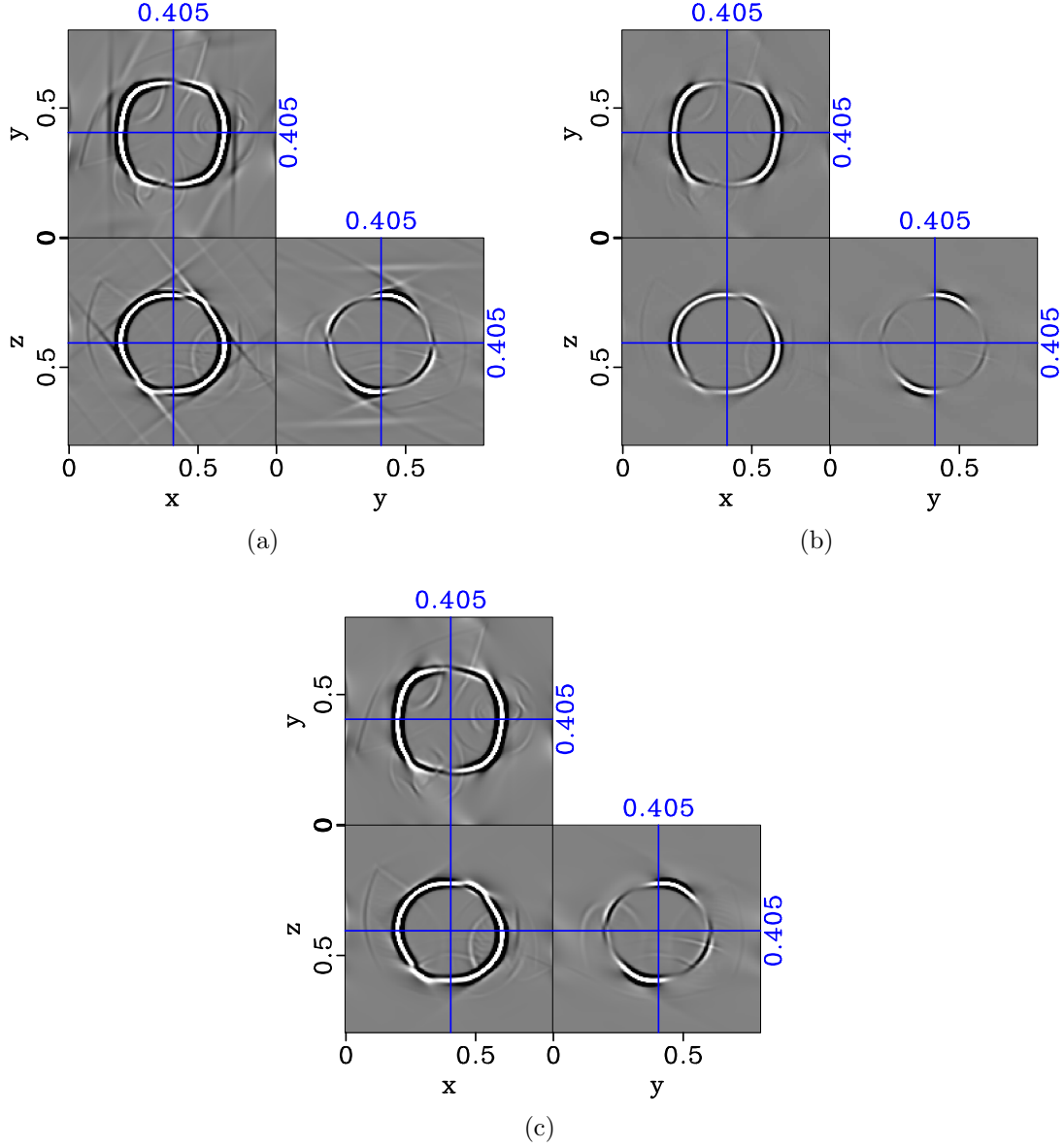
Figure 16: Separated y-component of S1 elastic wavefield in the two-layered heteroge-nous triclinic model (equation 29) with τ equal to a) 0 (no smoothing) b) 0.2. The final seprated wavefield with amplitude compensation (equation 28) is shown in c). Notice planar artifacts disappearing when the proposed smoothing filter is applied as shown in b) and with the restored amplitude asshown in c). The clipping has been adjusted to enhance visualization and stay constant in all three plots.
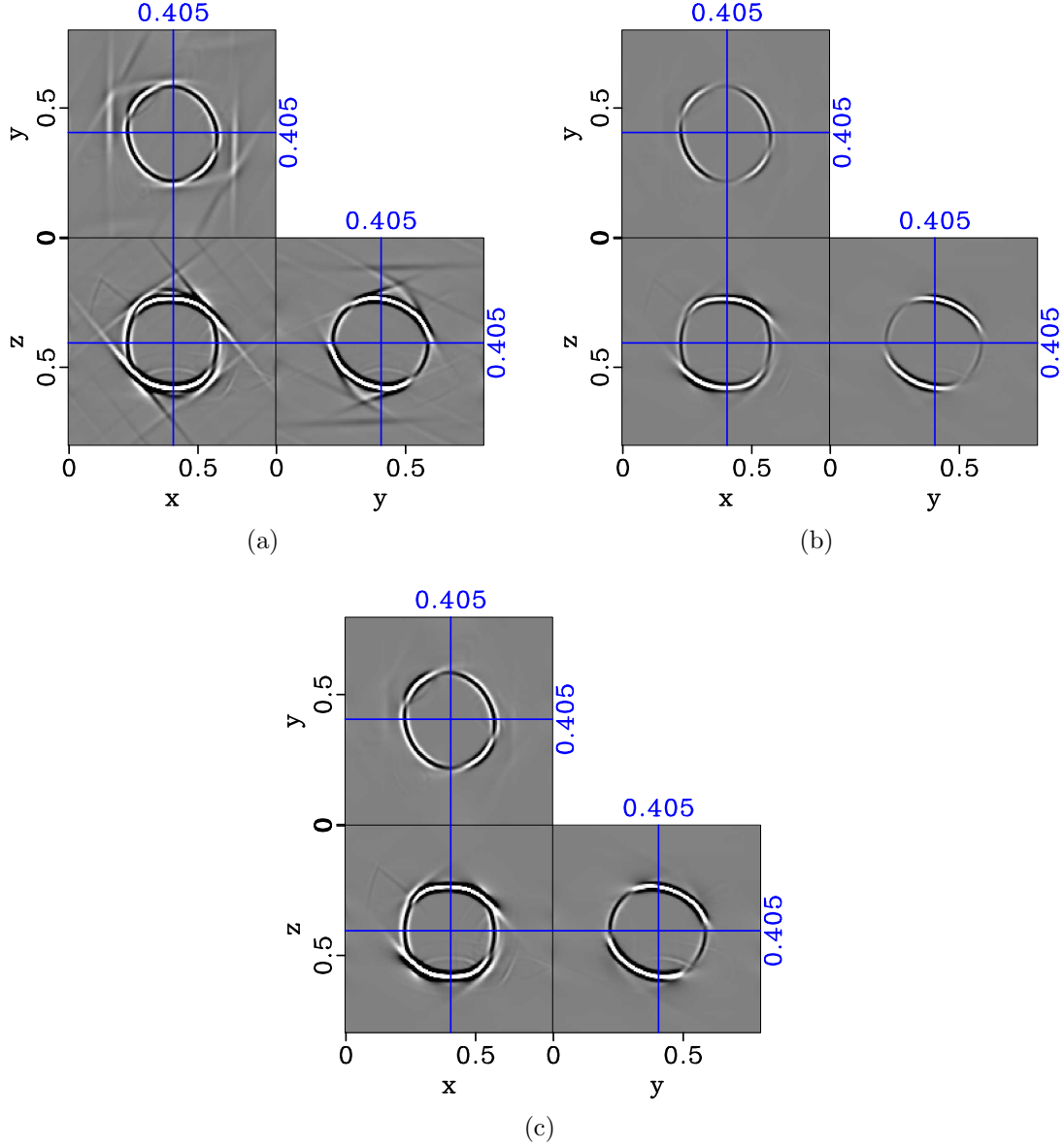
(a)

(b)

(c)

Figure 17: Separated y-component of S2 elastic wavefield in the two-layered heterogenous triclinic model (equation 29) with τ equal to a) 0 (no smoothing) b) 0.2. The final seprated wavefield with amplitude compensation (equation 28) is shown in c). Notice planar artifacts disappearing when the proposed smoothing filter is applied as shown in b) and with the restored amplitude as shown in c). The clipping has been adjusted to enhance visualization and stay constant in all three plots.

CONCLUSIONS

We have extended the method of elastic wave-vector decomposition to general heterogeneous anisotropic media. The simplest way to define the two S modes in such media is to sort them based on the magnitude of their phase velocities. However, this creates difficulties for wave-mode separation and wave-vector decomposition because of the polarization discontinuity at the singularities where the S modes are not easily separable. Using an analytical expression for locating the S-wave singularities in low-symmetry media, we propose to calculate the proximity to the singularity at a given phase direction and to define the area in which a filtering can be applied to reduce the planar artifacts caused by the local discontinuity of polarization vectors at the singularities. The amplitudes affected by the filtering process are additionally compensated by the technique of local signal-noise orthogonalization. Our computational experiments confirm that the proposed method presents an effective way to separate wavefields corresponding to each of the three wave modes in heterogenous anisotropic media. It is appropriate in applications to true-amplitude seismic imaging and inversion.

ACKNOWLEDGMENTS

APPENDIX: REVIEW OF CHRISTOFFEL EQUATION

The wave-mode separation and wave-vector decomposition methods discussed in the previous sections are based on polarization vectors of wave modes in anisotropic media. Polarization vectors can be found from the Christoffel equation given by

$$\left[\mathbf{G} - \rho v^2 \mathbf{I}\right] \mathbf{a} = 0 \ , \tag{A-1}$$

where $\mathbf{G}$ denotes the Christoffel matrix $G_{ij} = c_{ijkl}n_j n_l$, in which c_{ijkl} is the stiffness tensor, and n_j and n_l are the normalized wave-vector components in the j and l directions: $\mathbf{n} = \bar{\mathbf{k}} = \mathbf{k}/|\mathbf{k}|$. v denotes the phase velocity of a given wave mode for the given phase direction ($\mathbf{n}$), and $\mathbf{a}$ denotes the corresponding polarization vector (Červený, 2001).

In the non-degenerate case, the Christoffel matrix $\mathbf{G}$ has three distinct eigenvalues and three corresponding eigenvectors. The eigenvectors represent the polarization vectors of the three wave modes (P and two S) with the corresponding eigenvalues indicating the squared phase velocities v^2 of the waves. In the degenerate case, any

two or all three eigenvalues become equal and the corresponding phase direction is referred to as the *singular* direction (Vavryčuk, 2001). Note that if two eigenvalues for S waves coincide for all phase directions, the problem reduces to isotropy, which is a special case of Christoffel degeneracy.

Wave propagation in low-symmetry anisotropic media involves at most twenty-one independent stiffness tensor coefficients in the case of triclinic media. The elements of general Christoffel matrix $\mathbf{G}$ can be defined as follows:

$$
\begin{aligned}
G_{11} &= c_{11}n_1^2 + c_{66}n_2^2 + c_{55}n_3^2 + 2c_{16}n_1n_2 + 2c_{15}n_1n_3 + 2c_{56}n_2n_3 \ , &\text{(A-2)}\\
G_{22} &= c_{66}n_1^2 + c_{22}n_2^2 + c_{44}n_3^2 + 2c_{26}n_1n_2 + 2c_{46}n_1n_3 + 2c_{24}n_2n_3 \ , \\
G_{33} &= c_{55}n_1^2 + c_{44}n_2^2 + c_{33}n_3^2 + 2c_{45}n_1n_2 + 2c_{35}n_1n_3 + 2c_{34}n_2n_3 \ , \\
G_{12} &= c_{16}n_1^2 + c_{26}n_2^2 + c_{45}n_3^2 + (c_{12} + c_{66})n_1n_2 + (c_{14} + c_{56})n_1n_3 + (c_{25} + c_{46})n_2n_3 \ , \\
G_{13} &= c_{15}n_1^2 + c_{46}n_2^2 + c_{35}n_3^2 + (c_{14} + c_{56})n_1n_2 + (c_{13} + c_{55})n_1n_3 + (c_{36} + c_{45})n_2n_3 \ , \\
G_{23} &= c_{56}n_1^2 + c_{24}n_2^2 + c_{34}n_3^2 + (c_{25} + c_{46})n_1n_2 + (c_{36} + c_{45})n_1n_3 + (c_{23} + c_{44})n_2n_3 \ .
\end{aligned}
$$

Equation A-2 reduces to the case of orthorhombic media when $c_{14} = c_{15} = c_{16} = c_{24} = c_{25} = c_{26} = c_{34} = c_{35} = c_{36} = c_{45} = c_{46} = c_{56} = 0$, and further to the case of TI media when, additionally, $c_{11} = c_{22}$, $c_{13} = c_{23}$, and $c_{44} = c_{55}$.

REFERENCES

Aki, K., and P. G. Richards, 2002, Quantitative seismology: University Science Books.

Bakulin, A., V. Grechka, and I. Tsvankin, 2000, Estimation of fracture parameters from reflection seismic data–Part II: Fractured models with orthorhombic symmetry: Geophysics, **65**, no. 6, 1803–1817.

Červený, V., 2001, Seismic ray theory: Cambridge University Press.

Chen, Y., and S. Fomel, 2015, Random noise attenuation using local signal-noise orthogonalization: Geophysics, **80**, no. 6, WD1–WD18.

Cheng, J., and S. Fomel, 2014, Fast algorithms for elastic-wave-mode separation and vector decomposition using low-rank approximation for anisotropic media: Geophysics, **79**, no. 4, C97–C110.

Cheng, J., and W. Kang, 2014, Simulating propagation of separated wave modes in general anisotropic media, Part I: qP-wave propagators: Geophysics, **79**, no. 1, C1–C18.

——, 2016, Simulating propagation of separated wave modes in general anisotropic media, Part II: qS-wave propagators: Geophysics, **81**, no. 2, C39–C52.

Crampin, S., 1984, An introduction to wave propagation in anisotropic media: Geophysical Journal of the Royal Astronomical Society, **76**, 17–28.

——, 1991, Effects of point singularities on shear-wave propagation in sedimentary basins: Geophysical Journal International, **107**, 531–543.

Crampin, S., and M. Yedlin, 1981, Shear-Wave Singularities of Wave Propagation in Anisotropic Media: Journal of Geophysics, **49**, 43–46.

Dellinger, J., and J. Etgen, 1990, Wave-field separation in two-dimensional anisotropic media: Geophysics, **55**, no. 7, 914–919.

Dellinger, J. A., 1991, Anisotropic Seismic Wave Propagation: PhD thesis, Stanford University.

Farra, V., and I. Pšenčík, 2003, Properties of zero-, first- and higher-order approximations of attributes of elastic waves in weakly anisotropic media: Journal of Acoustical Society of America, **114**, 1366–1378.

Fomel, S., L. Ying, and X. Song, 2013, Seismic wave extrapolation using low rank symbol approximation: Geophysical Prospecting, **52**, 526–536.

French, W. S., 1974, Two-dimensional and three-dimensional migration of model-experiment reflection profiles: Geophysics, **39**, no. 3, 265–277.

Grechka, V., 2009, Applications of seismic anisotropy in the oil and gas industry: European Association of Geoscientists and Engineers.

Mah, M., and D. R. Schmitt, 2003, Determination of the complete elastic stiffnesses from ultrasonic phase velocity measurements: Journal of Geophysical Research, **108**, no. B1, ECV6 1–11.

Schoenberg, M., and K. Helbig, 1997, Orthorhombic media: Modeling elastic wave behavior in a vertically fractured earth: Geophysics, **62**, 1954–1974.

Sripanich, Y., and S. Fomel, 2015, On anelliptic approximations for qP velocities in transversely isotropic and orthorhombic media: Geophysics, **80**, no. 5, C89–C105.

Sripanich, Y., S. Fomel, and P. Fowler, 2016, A comparison of anisotropic parameterization for TI and orthorhombic media and their sensitivity with respect to

qP velocities: 86th Annual International Meeting Expanded Abstracts, Society of Exploration Geophysicists, 479–484.

Sripanich, Y., S. Fomel, J. Sun, and J. Cheng, 2015, Elastic wave-vector decomposition in orthorhombic media: 85th Annual International Meeting Expanded Abstracts, Society of Exploration Geophysicists, 498–503.

Sun, J., S. Fomel, Y. Sripanich, and P. Fowler, 2016a, Elastic wave extrapolation in strongly heterogeneous anisotropic media: Presented at the 17th Internation Workshop on Seismic Anisotropy.

——, 2016b, Recursive integral time extrapolation of elastic waves using lowrank approximation: 86th Annual International Meeting Expanded Abstracts, Society of Exploration Geophysicists, 4145–4151.

Thomsen, L., 2014, Understanding seismic anisotropy in exploration and exploitation, 2 ed.: Society of Exploration Geophysicists and European Association of Geoscientists and Engineers.

Tsvankin, I., 1997, Anisotropic parameters and P-wave velocity for orthorhombic media: Geophysics, **62**, 1292–1309.

——, 2012, Seismic signatures and analysis of reflection data in anisotropic media: Society of Exploration Geophysicists.

Tsvankin, I., and V. Grechka, 2011, Seismology of Azimuthally Anisotropic Media and Seismic Fracture Characterization: Society of Exploration Geophysicists.

Vasconcelos, I., and I. Tsvankin, 2006, Non-hyperbolic moveout inversion of wide-azimuth P-wave data for orthorhombic media: Geophysical Prospecting, **54**, 535–552.

Vavryčuk, V., 2001, Ray tracing in anisotropic media with singularities: Geophysical Journal International, **145**, 265–276.

Wang, C., J. Cheng, and B. Arntsen, 2016, Scalar and vector imaging based on wave mode decoupling for elastic reverse time migration in isotropic and TI media: Geophysics, **81**, no. 5, S383–S398.

Wang, T., J. Cheng, and C. Wang, 2015, Elastic wave mode decoupling for full waveform inversion: Presented at the 77th Annual EAGE Meeting Expanded Abstracts, EAGE.

Xu, X., I. Tsvankin, and A. Pech, 2005, Geometrical spreading of P-waves in horizontally layered, azimuthally anisotropic media: Geophysics, **70**, D43–D53.

Yan, J., and P. Sava, 2008, Isotropic angle-domain elastic reverse-time migration: Geophysics, **73**, no. 6, 8229–8239.

——, 2009, Elastic wave-mode separation for VTI media: Geophysics, **74**, no. 5, WB19–WB32.

——, 2011, Improving the efficiency of elastic wave-mode separation for heterogeneous tilted transverse isotropic media: Geophysics, **76**, no. 4, T65–T78.

——, 2012, Elastic wave mode separation for tilted transverse isotropic media: Geophysical Prospecting, **60**, 29–48.

Zhang, Q., and G. A. McMechan, 2010, 2D and 3D elastic wavefield vector decomposition in the wavenumber domain for VTI media: Geophysics, **75**, no. 3, D13–D26.